

# Pyramidal resistor networks for electrical impedance tomography with partial boundary measurements.

L. Borcea<sup>1</sup>, V. Druskin<sup>2</sup>, A.V. Mamonov<sup>1</sup> and F. Guevara Vasquez<sup>3</sup>

<sup>1</sup>Computational and Applied Mathematics, Rice University,  
MS 134, 6100 Main St. Houston, TX 77005-1892, USA

<sup>2</sup>Schlumberger Doll Research Center,  
One Hampshire St., Cambridge, MA 02139-1578, USA

<sup>3</sup>Department of Mathematics, University of Utah,  
155 S 1400 E RM 233, Salt Lake City, UT 84112-0090, USA

E-mail: borcea@rice.edu, druskin1@slb.com, mamon@rice.edu and  
fguevara@math.utah.edu

**Abstract.** We introduce an inversion algorithm for electrical impedance tomography (EIT) with partial boundary measurements, in two dimensions. It gives stable and fast reconstructions using sparse parameterizations of the unknown conductivity on optimal grids that are computed as part of the inversion. We follow the approach in [8, 27] that connects inverse discrete problems for resistor networks to continuum EIT problems, using optimal grids. The algorithm in [8, 27] is based on circular resistor networks, and solves the EIT problem with full boundary measurements. It is extended in [11] to EIT with partial boundary measurements, using extremal quasiconformal mappings that transform the problem to one with full boundary measurements. Here we introduce a different class of optimal grids, based on resistor networks with pyramidal topology, that is better suited for the partial measurements setup. We prove the unique solvability of the discrete inverse problem for these networks, and develop an algorithm for finding them from the measurements of the DtN map. Then, we show how to use the networks to define the optimal grids and to approximate the unknown conductivity. We assess the performance of our approach with numerical simulations and compare the results with those in [11].

## 1. Introduction.

We present a novel approach for the numerical approximation of solutions of electrical impedance tomography (EIT) with partial boundary measurements, in two dimensions. The EIT problem [13, 6] is to find the conductivity  $\sigma(x)$  in a simply connected domain  $\Omega \subset \mathbb{R}^2$ , given simultaneous measurements of currents and voltages at the boundary  $\mathcal{B}$  of  $\Omega$ . More explicitly,  $\sigma(x)$  is the coefficient in the elliptic equation

$$\nabla \cdot (\sigma(x) \nabla u(x)) = 0, \quad x \in \Omega, \quad (1.1)$$

with Dirichlet boundary conditions

$$u(x) = \phi(x), \quad x \in \mathcal{B}, \quad (1.2)$$

and it is to be determined from measurements of the Dirichlet to Neumann (DtN) map  $\Lambda_\sigma : H^{1/2}(\mathcal{B}) \rightarrow H^{-1/2}(\mathcal{B})$ , where

$$\Lambda_\sigma \phi(x) = \sigma(x) \frac{\partial u}{\partial \nu}(x), \quad x \in \mathcal{B}, \quad (1.3)$$

and  $\nu$  is the outer unit normal at  $\mathcal{B}$ .

EIT with full boundary measurements refers to the ideal case with complete knowledge of the DtN map. It is uniquely solvable as proved in [40, 12] under some regularity assumptions on  $\sigma$ , and in [3] for bounded  $\sigma$ . We consider the EIT problem with partial boundary measurements on the *accessible* subset  $\mathcal{B}_A$  of  $\mathcal{B}$ . The *inaccessible* boundary  $\mathcal{B}_I = \mathcal{B} \setminus \mathcal{B}_A$  is assumed grounded. That  $\sigma$  is determined uniquely by the set of Cauchy data  $\left\{ u|_{\mathcal{B}_A}, \sigma \frac{\partial u}{\partial \nu}|_{\mathcal{B}_A} \right\}$ , when  $u|_{\mathcal{B}_I} = 0$ , follows from [19, 20, 34, 35] for real-analytic or piecewise real-analytic  $\sigma$ , and from [28] for  $\sigma \in C^{3+\epsilon}(\bar{\Omega})$ , with  $\epsilon > 0$ .

Because we are concerned with numerical inversion, we work with finitely many measurements<sup>‡</sup> of the DtN map. Still, we say that we have a full boundary data EIT problem when the measurement points are distributed on the entire boundary  $\mathcal{B}$ . The partial data problem considered in this paper has the measurement points confined to the accessible boundary  $\mathcal{B}_A$ , which is a proper subset of  $\mathcal{B}$ .

The uniqueness and stability of numerical estimates (images) of  $\sigma$  are highly dependent on their parametrization. Naturally, the number of degrees of freedom in the measurements limits the number of parameters that we can recover. However, the real difficulty is caused by the exponential ill-posedness of the underlying continuum EIT problem, even in the ideal case of complete knowledge of the DtN map. By exponential instability we mean that the sup norm of perturbations of  $\sigma$  is bounded in terms of the logarithm of the operator norm of perturbations of  $\Lambda_\sigma$  [1, 5, 33]. The bounds are sharp [38], but the estimates are global and do not give resolution limits of the images of  $\sigma(x)$  as we vary  $x \in \Omega$ .

The trade-off between stability and resolution is studied in [2, 32, 41] for linearized, full boundary data EIT. The results in [2] give explicit reconstructions of small perturbations  $\delta\sigma$  of a constant conductivity, which are then used to assess the stability and resolution. The distinguishability studies in [32, 41] do not look for small perturbations, but are still linear in the sense that they determine the smallest support of a single inclusion centered at a given  $x \in \Omega$ , in a constant conductivity background, that causes visible perturbations of the boundary data. Both approaches lead to the intuitive conclusion that stability comes at the cost of progressive loss of resolution as we move away from the boundary, where the measurements are made. This means that if we use inadequate parameterizations of the unknown  $\sigma$ , on grids that are too fine inside  $\Omega$ , the numerical inversion will be unstable and must be regularized [24].

The question is then how to find proper parameterizations of  $\sigma$ , on grids that capture correctly the resolution limits, to get stable images without additional regularization that typically requires prior information about  $\sigma$ . The distinguishability grids proposed in [32] (see also [37, 36]) capture qualitatively the loss of resolution, but they are defined with a linearization approach whose accuracy is not understood. Here we follow the ideas in [8, 27, 11] and parametrize  $\sigma$  on *optimal* grids that are computed as part of the problem. The name optimal refers to the fact that finite volume discretizations of (1.1)–(1.2) on these sparse grids give spectrally accurate approximations of the DtN map. The computed grids turn out to be refined near the

<sup>‡</sup> By measurements we mean a measurement operator that takes the DtN map to a discrete data set at the measurement points on  $\mathcal{B}$ , as explained in section 2.3.

accessible boundary, where we make the measurements, and are coarse away from it, thus capturing the expected loss of resolution of the images.

Optimal grids were introduced and analyzed in [4, 21, 22, 30] for forward problems. Then, they were used in [7] for Sturm-Liouville inverse spectral problems in one dimension. The main result there is that parameterizations on optimal grids are necessary and sufficient for convergence of solutions of discrete inverse spectral problems to the true solution of continuum problems. The first inversion method on optimal grids for two dimensional EIT was proposed and analyzed in [8, 27], for the case of full boundary measurements. It is based on the rigorous theory of discrete inverse problems for *circular resistor networks* developed in [14, 15, 29, 17, 18]. These networks arise in five point stencil finite volumes discretizations of (1.1)–(1.2), on the optimal grids. The networks are *critical*, which means that they have no redundant connections and are determined uniquely by the discrete measurements of  $\Lambda_\sigma$ .

As in [8, 27], our inversion method consists of two steps. In the first step, we use the optimal grids and the solution of the discrete inverse problem for networks to define a nonlinear *reconstruction* mapping  $\mathcal{Q}_n$  from the boundary measurements to the space of conductivity functions. The mapping is called a reconstruction because it is an approximate inverse of the forward map that takes  $\sigma$  to the boundary data. In the second step of the inversion we use  $\mathcal{Q}_n$  as a preconditioner in a Gauss-Newton iteration for estimating  $\sigma$ , which typically converges in one or two steps [8, 27]. This second step is the same for full or partial boundary measurements. It is studied in detail in [8, 27], and we do not repeat it here. The interesting part is the definition of the optimal grids and therefore of the mapping  $\mathcal{Q}_n$ , which depends strongly on the measurement setup.

### 1.1. Motivation and outline of the results in this paper.

So far, the construction of the optimal grids has remained essentially one dimensional. This is the case for the grids introduced in [4, 21, 22, 30] for forward problems, and for the grids introduced in [8, 27] for two dimensional full boundary data EIT, with equidistantly distributed measurement points on  $\mathcal{B}$ . In all these studies, the grid construction relies on the rotational symmetry of the problem with constant  $\sigma$ , and uses Fourier transforms in all but the depth (radial) variable. The problem is then reduced to finding the optimal placement of the points along one direction, and can be cast nicely in terms of rational approximations of the transformed DtN map.

The EIT problem with partial measurements is not rotationally invariant, so it is not immediately clear how to use the ideas in [8, 27] to define the optimal grids. The recovery of networks with topology given in [8, 27] works the same for any placement of the boundary (measurement) nodes on the entire  $\mathcal{B}$ , or on proper subsets  $\mathcal{B}_A \subset \mathcal{B}$ . The problem is that when we use the approach in [8, 27] to build the grid piece by piece, starting from  $\mathcal{B}_A$ , we do not get a good result. More explicitly, the grid lines are far from orthogonal at their intersection, and finite volumes discretizations on them have poor approximation properties of the DtN map for non constant  $\sigma$ .

The confinement of the measurement points to the accessible boundary  $\mathcal{B}_A$  induces a coordinate transformation, which must be understood in order to define the grids. This is done in [11] with conformal or extremal quasiconformal mappings that take the boundary points in  $\mathcal{B}_A$  to equidistantly distributed points on  $\mathcal{B}$ . Then, the grids for the transformed problem are computed with the approach in [8, 27]. The coordinate transformations used in [11] are conformal or extremally quasiconformal

to ensure that the transformed conductivity remains isotropic, or at least to minimize its anisotropy. Otherwise, the EIT problem in the transformed coordinates does not have a unique solution and the resulting grids do not give good approximations of  $\sigma$ .

The results in [11] show a trade-off between having undistorted images and resolution distributed throughout  $\Omega$ . To eliminate distortions, the transformed conductivity should remain isotropic, which means that the coordinate transformation must be conformal. However, the resulting grids have poor refinement properties, with node accumulation in the vicinity of the center of  $\mathcal{B}_A$ , and very poor resolution of the images in the remainder of  $\Omega$ . The conformal mappings also require a rigid placement of the measurement points on  $\mathcal{B}_A$ . The extremal quasiconformal grids achieve a more uniform resolution in  $\Omega$ , and allow the arbitrary placement of the measurement points on  $\mathcal{B}_A$ . However, they induce artifacts in the images because the transformed conductivity is anisotropic.

The observation that motivates the results in this paper is that the topology of the networks used in [8, 27, 11] is not the best one for the partial measurement setup. It is because of it and the essential one dimensional nature of the grids, that we get the trade-off studied in [11]. Our main result in this paper is the introduction of truly two dimensional optimal grids, with *pyramidal* topology, that is naturally suited for the partial measurements setup. We prove the unique solvability of the discrete inverse problem for the underlying pyramidal resistor networks, and give an explicit layer peeling algorithm for determining them from the partial measurements of  $\Lambda_\sigma$ . The algorithm is very fast, and can be regularized by restricting the number of resistors, thus ensuring the sparsity of the resulting grids. We also define the reconstruction mapping  $\mathcal{Q}_n$  on the pyramidal optimal grids, and show with numerical simulations that it is superior to the reconstructions in [11].

The paper is organized as follows. We begin in section 2 with the formulation of the discrete EIT problem for resistor networks and a brief review of results from [14, 15, 29, 17, 18] and [8, 27, 11]. We include this review to explain where the results of this paper enter the basic inversion algorithm. Our new results are in the remaining sections 3-5. We prove the solvability of the inverse problem on pyramidal networks in section 3, and give an algorithm for finding them. Then, we define in section 4 the optimal grids and the reconstruction mapping. The numerical results are in section 5. We end with a summary in section 6.

## 2. Electrical impedance tomography with resistor networks.

Our goal is to develop a robust and fast numerical algorithm for approximating the solution of the continuum EIT problem with partial data, which seeks the scalar valued, positive and bounded conductivity function  $\sigma(x)$ , given the Cauchy data set

$$\mathcal{C}_\sigma = \left\{ \left( u|_{\mathcal{B}_A}, \sigma \frac{\partial u}{\partial \nu} \Big|_{\mathcal{B}_A} \right) \mid \nabla \cdot (\sigma(x) \nabla u(x)) = 0, x \in \Omega, u|_{\mathcal{B}_I} = 0 \right\}. \quad (2.1)$$

The algorithm makes the connection between discrete inverse problems for resistor networks and continuum EIT, using the optimal grids. We begin in section 2.1 with the formulation of the discrete EIT problem for networks, and we cite from [14, 15, 29, 17, 18] the necessary and sufficient conditions for its unique solvability. We motivate the networks in the context of finite volume discretizations of (1.1)–(1.2) in section 2.2. Then, we discuss the connection between the continuum and the discrete inverse problem in sections 2.3 and 2.5.

## 2.1. The inverse problem for resistor networks.

A *resistor network* is a pair  $(\Gamma, \gamma)$ , where  $\Gamma = (Y, E)$  is a graph with vertices (nodes)  $Y$  and edges  $E \subset Y \times Y$ , and  $\gamma : E \rightarrow \mathbb{R}^+$  is a positive valued *conductance* function. The set  $Y$  is the union of two disjoint sets  $Y_B$  and  $Y_I$  of *boundary* and *interior* vertices. We let

$$n = |Y_B| \quad (2.2)$$

be the number of boundary nodes, and use hereafter the symbol  $|\cdot|$  to denote the cardinality of finite sets.

Define a potential function  $u : Y \rightarrow \mathbb{R}$  and denote by  $u_B$  and  $u_I$  its restriction to the boundary and interior nodes. The potential satisfies Kirchhoff's node law

$$\begin{bmatrix} K_{II} & K_{IB} \\ K_{BI} & K_{BB} \end{bmatrix} \begin{bmatrix} u_I \\ u_B \end{bmatrix} = \begin{bmatrix} 0 \\ J_B \end{bmatrix}, \quad (2.3)$$

where  $J_B \in \mathbb{R}^n$  is the vector of currents through the boundary nodes, and  $K$  is the symmetric matrix

$$K_{ij} = \begin{cases} -\gamma[(v_i, v_j)], & \text{if } i \neq j \text{ and } (v_i, v_j) \in E, \\ 0, & \text{if } i \neq j \text{ and } (v_i, v_j) \notin E, \\ \sum_{k:(v_i, v_k) \in E} \gamma[(v_i, v_k)], & \text{if } i = j. \end{cases} \quad (2.4)$$

We write in (2.3) the block structure of  $K$ , using the notation  $K_{XZ}$  for the block with row indices in  $X \subseteq Y$  and column indices in  $Z \subseteq Y$ .

The DtN map of the network is the matrix  $\Lambda_\gamma \in \mathbb{R}^{n \times n}$  that takes  $u_B$  to  $J_B$ . It equals the Schur complement of  $K_{II}$

$$\Lambda_\gamma = K_{BB} - K_{BI}K_{II}^{-1}K_{IB}, \quad (2.5)$$

which is well defined for non singular  $K_{II}$ . As long as the network has a connected graph $\S$ , the invertability of  $K_{II}$  follows from the discrete analogue of the maximum principle, as shown in [14, 15, 16].

The discrete inverse problem is: Given a network with known graph  $\Gamma$  and DtN map  $\Lambda_\gamma$ , find its conductance function  $\gamma$ .

*2.1.1. Well connected planar circular graphs.* We study EIT in two dimensions, in a simply connected domain  $\Omega$  in  $\mathbb{R}^2$ . By the Riemann mapping theorem, all such sets are conformally equivalent, so we can think from now of  $\Omega$  as the unit disk in  $\mathbb{R}^2$ . Thus, it is natural to consider networks with *circular planar* graphs  $\Gamma$  which can be embedded in the plane, without self-intersections of the edges, in such a way that all interior nodes are in the unit disk, and the boundary nodes are on the unit circle.

Following [14, 15, 16], we number the boundary nodes  $Y_B = \{v_1, \dots, v_n\}$  so that they appear in a circular (clockwise or counterclockwise) order on  $\mathcal{B}$ . Consider a pair  $(P; Q)$  of subsets of  $Y_B$ , with  $P = \{v_{i_1}, \dots, v_{i_k}\}$ ,  $Q = \{v_{j_1}, \dots, v_{j_1}\}$  belonging to disjoint arcs of  $\mathcal{B}$ . The pair is called *circular* if the nodes  $\{v_{i_1}, \dots, v_{i_k}; v_{j_1}, \dots, v_{j_1}\}$  appear in circular order on  $\mathcal{B}$ .

A circular pair  $(P; Q)$  is called *connected*, if there exist  $k$  disjoint paths  $\alpha_s$  connecting  $v_{i_s}$  and  $v_{j_s}$ ,  $s = 1, \dots, k$ . The boundary nodes are allowed in  $\alpha_s$  only as the first and the last nodes (the paths must not touch the boundary). We let  $\pi(\Gamma)$  be the set of all connected circular pairs, and we say that the graph is *well connected* if all circular pairs are in  $\pi(\Gamma)$ .

$\S$  We say that the graph  $\Gamma = (Y, E)$  is connected when each pair of vertices in  $Y$  is connected by at least one set of edges in  $E$ .

*2.1.2. Solvability of the discrete inverse problem for networks.* The question of whether the discrete inverse problem is uniquely solvable is closely related to the topology of the graph  $\Gamma$ . For circular planar graphs, the question was resolved in [15], using the theory of *critical networks*.

Let  $\Gamma'$  be the graph obtained by removing one edge in  $\Gamma = (Y, E)$ . The edge can be removed by deletion or by contraction. Then, the network with graph  $\Gamma$  is called *critical* if removing any edge breaks some connection in  $\pi(\Gamma)$ , i.e.  $\pi(\Gamma') \subset \pi(\Gamma)$ .

It is shown in [15] that the discrete inverse problem for a network with given circular planar graph has a unique solution if and only if it is critical and the data matrix  $\Lambda_\gamma$  belongs to the set  $\mathcal{D}_n$  of DtN maps of well connected networks. The set  $\mathcal{D}_n$  is defined in [15]. It consists of all symmetric matrices  $\Lambda_\gamma \in \mathbb{R}^{n \times n}$  satisfying the conservation of currents condition

$$\Lambda_\gamma \mathbf{1} = \mathbf{0}, \quad (2.6)$$

and whose *circular minors* are totally non-positive. A circular minor of  $\Lambda_\gamma$  is a submatrix  $(\Lambda_\gamma)_{PQ}$  with row indices in  $P$  and column indices in  $Q$ , where  $(P; Q)$  is a circular pair. The total non-positivity means that

$$\det [-(\Lambda_\gamma)_{PQ}] \geq 0. \quad (2.7)$$

Equality in (2.7) occurs if and only if  $(P; Q) \notin \pi(\Gamma)$ . Thus, in a well connected network the inequality (2.7) is strict for every circular pair  $(P; Q)$ .

## 2.2. Resistor networks and finite volume discretizations.

Resistor networks can be motivated in the context of finite volume discretizations of (1.1)–(1.2) on staggered grids. Such grids consist of intersecting primary and dual grid lines, which are allowed to be curvilinear. We refer to the intersections of primary (dual) grid lines as the primary (dual) grid nodes. The potential  $u$  is discretized at the primary grid nodes, while the current fluxes  $\sigma \nabla u$  are discretized at the dual grid nodes.

We illustrate in figure 1 the vicinity of an interior primary grid node  $P_{i,j}$ . Let  $C_{i,j}$  be the dual grid cell with boundary

$$\partial C_{i,j} = \Sigma_{i,j+\frac{1}{2}} \cup \Sigma_{i+\frac{1}{2},j} \cup \Sigma_{i,j-\frac{1}{2}} \cup \Sigma_{i-\frac{1}{2},j}, \quad (2.8)$$

the union of the four dual grid segments

$$\Sigma_{i,j\pm\frac{1}{2}} = \left( P_{i-\frac{1}{2},j\pm\frac{1}{2}}, P_{i+\frac{1}{2},j\pm\frac{1}{2}} \right), \quad \Sigma_{i\pm\frac{1}{2},j} = \left( P_{i\pm\frac{1}{2},j-\frac{1}{2}}, P_{i\pm\frac{1}{2},j+\frac{1}{2}} \right).$$

We integrate (1.1) over  $C_{i,j}$ , and use the divergence theorem to obtain the balance of fluxes across the boundary  $\partial C_{i,j}$

$$\int_{C_{i,j}} \nabla \cdot (\sigma \nabla u) dV = \left( \int_{\Sigma_{i,j+\frac{1}{2}}} + \int_{\Sigma_{i+\frac{1}{2},j}} + \int_{\Sigma_{i,j-\frac{1}{2}}} + \int_{\Sigma_{i-\frac{1}{2},j}} \right) \sigma \frac{\partial u}{\partial \nu} dS = 0. \quad (2.9)$$

The linear algebraic system of equations for the discretized potential is obtained by approximating the boundary integrals in (2.9) with a one-point quadrature rule, and the normal derivatives in the integrands with a two point finite difference. We have

$$\int_{\Sigma_{i,j\pm\frac{1}{2}}} \sigma \frac{\partial u}{\partial \nu} dS \approx \sigma(P_{i,j\pm\frac{1}{2}}) \frac{L(\Sigma_{i,j\pm\frac{1}{2}})}{L(\Pi_{i,j\pm\frac{1}{2}})} [u(P_{i,j\pm 1}) - u(P_{i,j})], \quad (2.10)$$

$$\int_{\Sigma_{i\pm\frac{1}{2},j}} \sigma \frac{\partial u}{\partial \nu} dS \approx \sigma(P_{i\pm\frac{1}{2},j}) \frac{L(\Sigma_{i\pm\frac{1}{2},j})}{L(\Pi_{i\pm\frac{1}{2},j})} [u(P_{i\pm 1,j}) - u(P_{i,j})], \quad (2.11)$$

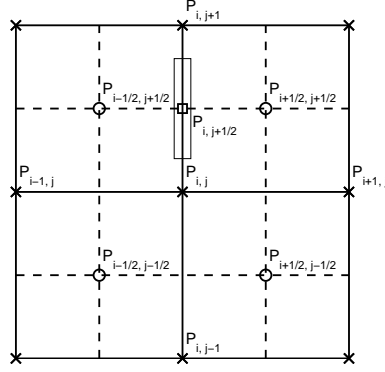


**Figure 1.** Vicinity of a primary node  $P_{i,j}$  in a staggered grid. The primary grid lines are solid, and the dual grid lines are dashed. The primary grid nodes are  $\times$  and the dual grid nodes are  $\circ$ . We show the resistor along the primary edge  $(P_{i,j+1}, P_{i,j})$  as a rectangle and denote by  $\square$  its intersection with the dual edge.

where  $P_{i,j \pm \frac{1}{2}}$  and  $P_{i \pm \frac{1}{2}, j}$  are the intersections of the primary grid segments

$$\Pi_{i,j \pm \frac{1}{2}} = (P_{i,j}, P_{i,j \pm 1}), \quad \Pi_{i \pm \frac{1}{2}, j} = (P_{i,j}, P_{i \pm 1, j})$$

with the dual grid segments  $\Sigma_{i,j \pm \frac{1}{2}}$  and  $\Sigma_{i \pm \frac{1}{2}, j}$ , as shown in figure 1. The arc lengths of the primary and dual grid segments are denoted by  $L(\Pi)$  and  $L(\Sigma)$ , respectively.

The algebraic system of equations for the discretized potential  $u_{i,j} \approx u(P_{i,j})$  is

$$\begin{aligned} \gamma_{i,j+\frac{1}{2}} (u_{i,j+1} - u_{i,j}) + \gamma_{i+\frac{1}{2},j} (u_{i+1,j} - u_{i,j}) + \\ \gamma_{i,j-\frac{1}{2}} (u_{i,j-1} - u_{i,j}) + \gamma_{i-\frac{1}{2},j} (u_{i-1,j} - u_{i,j}) = 0, \end{aligned} \quad (2.12)$$

where

$$\gamma_{\alpha,\beta} = \sigma(P_{\alpha,\beta}) \gamma_{\alpha,\beta}^{(1)}, \quad (2.13)$$

$$(\alpha, \beta) \in \left\{ \left( i, j + \frac{1}{2} \right), \left( i + \frac{1}{2}, j \right), \left( i, j - \frac{1}{2} \right), \left( i - \frac{1}{2}, j \right) \right\}, \quad (2.14)$$

and

$$\gamma_{\alpha,\beta}^{(1)} = \frac{L(\Sigma_{\alpha,\beta})}{L(\Pi_{\alpha,\beta})} \quad (2.15)$$

corresponds to the constant conductivity  $\sigma \equiv 1$ . This is Kirchhoff's node law for the resistor network with graph  $\Gamma = (Y, E)$  given by the primary grid. The set  $Y$  consists of the primary grid nodes and the edges in  $E$  are the primary grid segments. The conductance function is defined in (2.13). For example,  $\gamma_{i,j+\frac{1}{2}}$  is the conductance of edge  $\Pi_{i,j+\frac{1}{2}} \in E$ .

### 2.3. From the continuum to the discrete DtN map.

To connect continuum EIT problems with inverse problems for networks, we relate the matrix valued DtN map  $\Lambda_\gamma$  of a network to the continuum DtN map  $\Lambda_\sigma$ , using linear measurement operators

$$\mathcal{M}_n : \left( H^{1/2}(\mathcal{B}) \rightarrow H^{-1/2}(\mathcal{B}) \right) \rightarrow \mathbb{R}^{n \times n}.$$

In [8, 27], the operators  $\mathcal{M}_n$  are defined with a set of  $n$  non-negative *measurement functions*  $\chi_j$  with disjoint supports on  $\mathcal{B}$ , and normalized by

$$\int_{\mathcal{B}} \chi_j(x) dS_x = 1, \quad j = 1, \dots, n. \quad (2.16)$$

We can think of them as modeling the support of electrodes attached to the boundary. The symmetric matrix  $\mathcal{M}_n(\Lambda_\sigma)$  has off-diagonal entries

$$(\mathcal{M}_n(\Lambda_\sigma))_{i,j} = \langle \chi_i, \Lambda_\sigma \chi_j \rangle, \quad i \neq j, \quad (2.17)$$

where  $\langle \cdot, \cdot \rangle$  is the duality pairing between  $H^{1/2}(\mathcal{B})$  and  $H^{-1/2}(\mathcal{B})$ , and the diagonal entries are given by

$$(\mathcal{M}_n(\Lambda_\sigma))_{i,i} = - \sum_{j \neq i} \langle \chi_i, \Lambda_\sigma \chi_j \rangle, \quad i = 1, \dots, n. \quad (2.18)$$

The latter ensures that  $\mathcal{M}_n(\Lambda_\sigma)$  satisfies the conservation of currents condition.

Alternatively, we can consider pointwise measurements of the DtN map. For a sufficiently regular  $\sigma$ , the first order pseudodifferential operator  $\Lambda_\sigma$  can be written in an integral form as

$$(\Lambda_\sigma \phi)(x) = \int_{\mathcal{B}} \mathcal{K}_\sigma(x, y) \phi(y) dS_y, \quad x \in \mathcal{B}, \quad (2.19)$$

where  $\mathcal{K}_\sigma(x, y)$  is a symmetric kernel continuous away from the diagonal [31]. The pointwise measurement operator  $\mathcal{M}_n$  is defined at the points  $x_j \in \mathcal{B}$ ,  $j = 1, \dots, n$ , by

$$(\mathcal{M}_n(\Lambda_\sigma))_{i,j} = \begin{cases} \mathcal{K}_\sigma(x_i, x_j), & i \neq j, \\ - \sum_{k \neq i} \mathcal{K}_\sigma(x_i, x_k), & i = j. \end{cases} \quad (2.20)$$

These definitions do not distinguish between the full or partial boundary measurement setups. The partial data case corresponds to  $\text{supp} \chi_j \subset \mathcal{B}_A$  for (2.17), or  $x_j \in \mathcal{B}_A$  for (2.20).

Other measurement operators that use more accurate electrode models, such as the ‘‘complete electrode’’ model [42] can be used in principle. The crucial question is whether the range of the operators belongs to the set  $\mathcal{D}_n$  of DtN maps of well connected networks. This is the case for the operators (2.20) and (2.17), as proved in [31] and [8, 27], respectively. Then, we can write that

$$\Lambda_\gamma = \mathcal{M}_n(\Lambda_\sigma), \quad (2.21)$$

and conclude based on the results reviewed in section 2.1.2, that there exists a unique network with given critical circular planar graph and DtN map  $\Lambda_\gamma$  [15, 18].

#### 2.4. Solving the discrete inverse problem.

Given  $\Lambda_\gamma \in \mathcal{D}_n$  and the graph  $\Gamma$ , we can find the network (the conductance function  $\gamma$ ), with either a direct invariant imbedding (layer peeling) method, or with optimization. We prefer the first approach, because it is fast and explicit. Optimization may be more robust, but it is computationally intensive and the algorithm may get stuck in local minima. In any case, both approaches become unstable as we increase the size (the number of edges) of the network. It is in general unclear how to regularize optimization methods for network recovery, because we cannot speak of regularity assumptions as is done, for example, in total variation regularization approaches for continuum EIT. We have tried in [10] a Gauss-Newton iterative optimization method regularized with an SVD truncation of the Jacobian.

All the results in this paper are with layer peeling, which we regularize by restricting  $n$ , i.e. the size of network, as follows. We solve a sequence of discrete inverse problems for increasing  $n$ , until our layer peeling method fails to produce positive conductances. Then we set  $n$  to the last but one value in the sequence, and accept as the solution of the inverse problem the non-negative conductance obtained from the DtN matrix  $\Lambda_\gamma = \mathcal{M}_n(\Lambda_\sigma)$ .

#### 2.5. From the discrete to the continuum inversion: the optimal grids.

Once we have determined the discrete conductance  $\gamma$ , the question is how to use it to approximate the conductivity  $\sigma$ , the solution of the continuum EIT problem. As shown in (2.13), we must also have information about the finite volumes grid to approximate  $\sigma(P_{\alpha,\beta})$  from the knowledge of  $\gamma_{\alpha,\beta}$ . This leads us to the construction of the optimal grids, which are computed from the resistor networks with the same graph and DtN map

$$\Lambda_{\gamma^{(1)}} = \mathcal{M}_n(\Lambda_1). \quad (2.22)$$

Here,  $\Lambda_1$  is the continuum DtN map for constant conductivity  $\sigma \equiv 1$ , and  $\gamma^{(1)}$  is the conductance (2.15).

Thus, the optimal grids are computed so that finite volumes discretizations compute  $\Lambda_{\gamma^{(1)}}$  exactly. Then, we can estimate the conductivity at points  $P_{\alpha,\beta}$ , the intersections of the primary and dual grid segments, by

$$\sigma(P_{\alpha,\beta}) \approx \frac{\gamma_{\alpha,\beta}}{\gamma_{\alpha,\beta}^{(1)}}. \quad (2.23)$$

The *reconstruction mapping*  $\mathcal{Q}_n : \mathcal{D}_n \rightarrow \mathcal{S}$  is defined on the set  $\mathcal{D}_n$  of discrete DtN maps, with values in  $\mathcal{S}$ , the set of positive and bounded conductivities. It takes the measurements  $\mathcal{M}_n(\Lambda_\sigma)$  to the piecewise linear interpolation of (2.23) on the optimal grid.

Finally, the images can be improved further using a Gauss-Newton iteration that minimizes the objective function

$$\mathcal{O}(\sigma^s) = \|\mathcal{Q}_n[\mathcal{M}_n(\Lambda_\sigma^s)] - \mathcal{Q}_n[\mathcal{M}_n(\Lambda_\sigma)]\|_2^2 \quad (2.24)$$

over search conductivities  $\sigma^s \in \mathcal{S}$ . Note that  $\mathcal{Q}_n$  is used here as a non-linear preconditioner of the forward map  $\mathcal{F}_n : \mathcal{S} \rightarrow \mathcal{D}_n$ , which takes  $\sigma^s \in \mathcal{S}$  to  $\mathcal{M}_n(\Lambda_\sigma^s)$ . How good a preconditioner  $\mathcal{Q}_n$  is depends on the extrapolation properties of the optimal grids. That is to say, how accurate does the finite volumes approximation of  $\mathcal{M}_n(\Lambda_\sigma)$  remain for a wide class of conductivity functions that include the constant

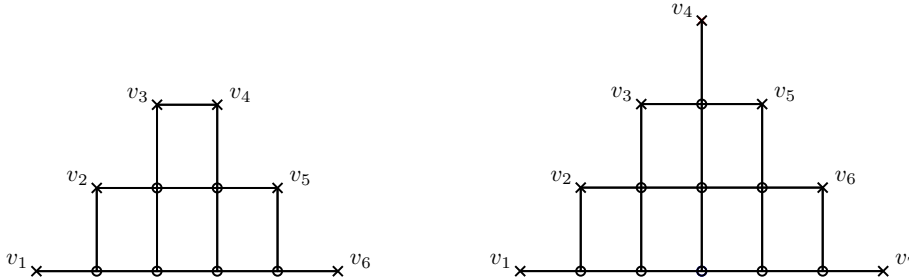


**Figure 2.** Pyramidal (standard) graphs  $\Gamma_n$ . Left:  $n = 6$ ; right:  $n = 7$ . Boundary nodes  $v_j, j = 1, \dots, n$  are  $\times$ , interior nodes are  $\circ$ .

$\sigma \equiv 1$ . Illustrations of the good extrapolation properties of optimal grids, for various measurement setups, are in [9, 8, 27, 7, 11].

There is only one part of the inversion algorithm outlined above that is sensitive to the measurement setup. It is the definition of the optimal grid, and therefore of the reconstruction mapping  $\mathcal{Q}_n$ . The optimization (2.24) is studied in detail in [8, 27] and we do not repeat it here. The remainder of this paper is concerned with reconstructions on a new class of truly two dimensional optimal grids, based on pyramidal resistor networks that are naturally suited to the partial measurements setup.

### 3. The inverse problem for pyramidal networks.

The pyramidal networks are also known in the literature under the name *standard*, since they can be chosen to be the representatives of certain classes of networks equivalent under  $Y - \Delta$  transformations [15]. Keeping the same notation as in the previous section, we denote the graphs of the pyramidal networks with  $n$  boundary nodes by  $\Gamma_n$ , and illustrate how they look in figure 2, for even and odd  $n$ . Hereafter, we refer to the edges of the graphs as “vertical” or “horizontal” according to their orientation in figure 2.

To use the pyramidal networks for inversion, we need to establish that they are uniquely recoverable from the DtN map, which is equivalent to showing that the graphs  $\Gamma_n$  are critical. We have the following result:

**Lemma 1.** *Pyramidal networks are critical.*

It is mentioned in [15, Proposition 7.3], without proof, that the networks  $\Gamma_n, n \geq 2$  are critical. We give the proof in Appendix A in the case of even  $n$ . The extension of the proof to odd  $n$  is straightforward.

#### 3.1. Layer peeling for pyramidal networks.

Now, let us show how to solve the inverse problem for the networks with pyramidal graphs  $\Gamma_n = (Y, E)$ , with a direct (layer peeling) algorithm that determines the conductance  $\gamma : E \rightarrow \mathbb{R}^+$  in a finite number of algebraic operations.

For the circular networks considered in [8, 27, 11], such an algorithm was developed in [14]. It is based on a concept of *special solutions*, which are the potentials arising from special choices of boundary data. These potentials limit the current flow

to a certain subset of edges of a network, so that the conductance of these edges can be recovered. The edges are then “peeled”, and the method proceeds deeper into the network, until the conductance of all edges is recovered.

Here we introduce a layer peeling algorithm for pyramidal networks with even number  $n$  of boundary nodes. The extension to odd  $n$  is possible.

**Algorithm 1.** *To determine the conductance  $\gamma$  of the pyramidal network  $(\Gamma_n, \gamma)$ , with given DtN map  $\Lambda_\gamma \in \mathcal{D}_n$ , take the following steps:*

- (1) *To compute the conductances of horizontal and vertical edges emanating from the boundary node  $v_p$ , for each  $p = 1, \dots, 2m$ , define the following sets:*

$$Z = \{v_1, \dots, v_{p-1}, v_{p+1}, \dots, v_m\}, C = \{v_{m+2}, \dots, v_{2m}\}, H = \{v_1, \dots, v_p\} \text{ and } V = \{v_p, \dots, v_{m+1}\}, \text{ in the case } p \leq m.$$

$$Z = \{v_{m+1}, \dots, v_{p-1}, v_{p+1}, \dots, v_{2m}\}, C = \{v_1, \dots, v_{m-1}\}, H = \{v_p, \dots, v_{2m}\} \text{ and } V = \{v_m, \dots, v_p\}, \text{ for } m+1 \leq p \leq 2m.$$

- (2) *Compute the conductance  $\gamma(e_{p,h})$  of the horizontal edge emanating from  $v_p$ , using*

$$\gamma(e_{p,h}) = \left( \Lambda_{p,H}^{(n)} - \Lambda_{p,C}^{(n)} \left( \Lambda_{Z,C}^{(n)} \right)^{-1} \Lambda_{Z,H}^{(n)} \right) \mathbf{1}_H, \quad (3.1)$$

where  $\mathbf{1}_H$  is a column vector of ones of size  $|H|$ .

Compute also the conductance  $\gamma(e_{p,v})$  of the vertical edge emanating from  $v_p$

$$\gamma(e_{p,v}) = \left( \Lambda_{p,V}^{(n)} - \Lambda_{p,C}^{(n)} \left( \Lambda_{Z,C}^{(n)} \right)^{-1} \Lambda_{Z,V}^{(n)} \right) \mathbf{1}_V. \quad (3.2)$$

- (3) *Once  $\gamma(e_{p,h})$ ,  $\gamma(e_{p,v})$  have been computed, peel the outer layer from  $\Gamma_n$  to obtain the subgraph  $\Gamma_{n-2}$  with the set  $S = \{w_1, \dots, w_{2m-2}\}$  of boundary nodes. Assemble the blocks  $K_S$ ,  $K_{SB}$ ,  $K_{BS}$ ,  $K_{BB}$  of the Kirchhoff matrix of  $(\Gamma_n, \gamma)$ , and compute the updated DtN map  $\Lambda^{(n-2)}$  of the network  $(\Gamma_{n-2}, \gamma)$ , as follows*

$$\Lambda^{(n-2)} = -K_S - K_{SB} P^T \left( P \left( \Lambda^{(n)} - K_{BB} \right) P^T \right)^{-1} P K_{BS}. \quad (3.3)$$

Here  $P \in \mathbb{R}^{(n-2) \times n}$  is a projection operator:  $PP^T = I_{n-2}$ , and the block  $K_S$  is defined in Appendix B from an appropriate splitting of the block  $K_{SS}$ .

- (4) *If  $m = 1$  terminate. Otherwise, decrease  $m$  by 1, update  $n = 2m$  and go back to step 1.*

The algorithm consists of two essential operations. First, in steps 1 and 2 we restrict the current flow to the edges  $e_{p,h}$  and  $e_{p,v}$  emanating from the boundary node  $v_p$  by means of special solutions  $u^{(p,h)}$  and  $u^{(p,v)}$  respectively. To define the special solutions we introduce the sets  $Z$ ,  $C$ ,  $H$  and  $V$ . The currents into the nodes in  $Z$  are set to zero. For  $u^{(p,h)}$  the potentials are set to one at  $H$  and to zero at  $Y_B \setminus (C \cup H)$ . For  $u^{(p,v)}$  the potentials are set to one at  $V$  and to zero at  $Y_B \setminus (C \cup V)$ . These conditions determine the special solutions uniquely. Then, the potential drop on  $e_{p,h}$  and  $e_{p,v}$  can be shown to be one, and thus their conductances are just the currents through  $v_p$ , which are given by formulas (3.1)–(3.2). Second, we peel the recovered layer in step 3, and compute the DtN map for the smaller network with graph  $\Gamma_{n-2}$ . Recursive application of these two operations recovers the whole network.

The theoretical justification of the algorithm is in the following theorem, proved in Appendix B.

**Theorem 1.** *The conductance  $\gamma$  of a pyramidal network  $(\Gamma_n, \gamma)$ , with  $n = 2m$ ,  $m \in \mathbb{N}$ , is uniquely recoverable from its DtN map  $\Lambda_\gamma^{(n)}$  by Algorithm 1.*

#### 4. Reconstruction on optimal grids.

Let us observe from (2.13)–(2.15) that once we know the conductances  $\gamma$  and  $\gamma^{(1)}$  of the networks with DtN maps (2.21) and (2.22), we can obtain the pointwise estimates (2.23) of  $\sigma$ . The remaining question addressed in this section is where to place these estimates in  $\Omega$ . We do not need full knowledge of the optimal grid, just the intersections  $P_{\alpha,\beta}$  of the primary and dual grid segments that appear in (2.23). Our approach is to estimate these points using the sensitivity analysis of both the continuum and the discrete problems, as we show below in sections 4.1–4.3.

##### 4.1. Kernel of the DtN map.

We begin the sensitivity analysis with the derivation of the expression of the kernel of the DtN map. We need the Dirichlet Green's function  $G(x, y)$ , the solution of

$$\nabla_x \cdot (\sigma(x) \nabla_x G(x, y)) = -\delta(x - y), \quad x \in \Omega, \quad (4.1)$$

with homogeneous Dirichlet boundary condition

$$G(x, y)|_{x \in \mathcal{B}} = 0, \quad (4.2)$$

where  $y \in \Omega$  is the *source* location.

Our numerical simulations are for domain  $\Omega = \mathbb{D}$  the unit disk, and  $\Omega = \mathbb{R}_-^2$  the lower half plane, respectively. In both cases we can write  $G(x, y)$  explicitly [26] when  $\sigma \equiv 1$ , as needed in the computation of the optimal grids. For  $\Omega = \mathbb{D}$  we have [26]

$$G_{\mathbb{D}}(x, y) = \frac{1}{2\pi} (-\log |x - y| + \log |y| (|x - \tilde{y}|)), \quad (4.3)$$

where  $\tilde{y} = y/|y|^2$  and  $|\cdot|$  is the Euclidean norm. When  $\Omega = \mathbb{R}_-^2$ ,

$$G_{\mathbb{R}_-^2}(x, y) = \frac{1}{2\pi} (-\log |x - y| + \log |x - \hat{y}|), \quad (4.4)$$

for  $\hat{y} = (I - 2\mathbf{e}_2\mathbf{e}_2^T)y$ ,  $I$  the  $2 \times 2$  identity matrix, and  $\mathbf{e}_2 = (0, 1)^T$ .

Consider a general  $\sigma$  that we assume regular enough to admit the integral representation (2.19) of the DtN map, and let us derive the expression of the kernel  $\mathcal{K}_\sigma(x, y)$  in terms of  $G(x, y)$ . Combining Green's second identity

$$\int_{\Omega} (f \nabla \cdot (\sigma \nabla g) - g \nabla \cdot (\sigma \nabla f)) dV = \int_{\mathcal{B}} \sigma \left( f \frac{\partial g}{\partial \nu} - g \frac{\partial f}{\partial \nu} \right) dS \quad (4.5)$$

for  $f = u(x)$ ,  $g = G(x, y)$ , with (4.1), (4.2), (1.1) and (1.2) we obtain

$$u(y) = - \int_{\mathcal{B}} \sigma(x) \phi(x) \nu(x) \cdot \nabla_x G(x, y) dS_x, \quad y \in \Omega. \quad (4.6)$$

Then, we can write, formally,

$$\sigma(y) \frac{\partial u}{\partial \nu} \Big|_{y \in \mathcal{B}} = - \int_{\mathcal{B}} \sigma(y) \sigma(x) (\nu(x) \cdot \nabla_x) (\nu(y) \cdot \nabla_y) G(x, y) \phi(x) dS_x, \quad (4.7)$$

and obtain

$$\mathcal{K}_\sigma(x, y) = -\sigma(x) \sigma(y) (\nu(x) \cdot \nabla_x) (\nu(y) \cdot \nabla_y) G(x, y), \quad x, y \in \mathcal{B}. \quad (4.8)$$

Note that although  $G(x, y)$  is not defined for  $y \in \mathcal{B}$ , equation (4.8) contains the normal derivative of  $G(x, y)$  with respect to  $y$ , which is well defined.

Differentiating (4.3) and (4.4) we obtain the kernel  $\mathcal{K}_1(x, y)$  of the DtN map for Laplace's equation in the unit disk and in the half plane, respectively. The Jacobian of  $\tilde{y}$  is given by

$$D_y(\tilde{y}) = \frac{I}{|y|^2} - \frac{2yy^T}{|y|^4}, \quad (4.9)$$

which allows us to compute

$$(\nu(y) \cdot \nabla) G_{\mathbb{D}}(x, y) = \frac{1}{2\pi} \left( 1 + 2y \cdot (\widetilde{x - y}) \right), \quad |y| = 1. \quad (4.10)$$

The second differentiation in conjunction with (4.9), (4.8) and  $|x| = |y| = 1$  gives

$$\mathcal{K}_1(x, y) = -\frac{1}{\pi|x - y|^2}. \quad (4.11)$$

The expression of the kernel in the case  $\Omega = \mathbb{R}_+^2$  is exactly the same. Moreover, formula (4.11) is valid for any region conformally equivalent to the unit disk. This follows from the invariance of the DtN map under conformal coordinate transformations [43].

The behavior of the kernel  $\mathcal{K}_\sigma(x, y)$  for general  $\sigma$  is similar to (4.11) in the sense that away from the diagonal  $x = y$ , it admits the representation [31]

$$\mathcal{K}_\sigma(x, y) = -\frac{k(x, y)}{\pi|x - y|^2}. \quad (4.12)$$

Here  $k(x, y)$  is a symmetric, positive continuous function on  $\mathcal{B} \times \mathcal{B}$ , that does not vanish on the diagonal.

#### 4.2. Sensitivity functions.

Given the kernel of the DtN map, we can now perform the sensitivity analysis with respect to the changes in  $\sigma$ . Since (4.8) gives  $\mathcal{K}_\sigma(x, y)$  in terms of the Green's function, we compute first the sensitivity of  $G(x, y)$ .

Let  $G(x, y) + \delta G(x, y)$  be the Green's function corresponding to the perturbed conductivity  $\sigma + \delta\sigma$ . To compute the sensitivity of  $G$ , it suffices to assume very small perturbations  $\delta\sigma$  and approximate  $\delta G(x, y)$  by the solution of the linearized equation

$$\begin{aligned} \nabla_x \cdot (\sigma(x) \nabla_x \delta G(x, y)) &= -\nabla_x \cdot (\delta\sigma(x) \nabla_x G(x, y)), \quad x \in \Omega, \\ \delta G(x, y) &= 0, \quad x \in \mathcal{B}. \end{aligned} \quad (4.13)$$

We have

$$\begin{aligned} \delta G(x, y) &= \int_{\Omega} G(x, s) \nabla_s \cdot (\delta\sigma(s) \nabla_s G(s, y)) ds, \\ &= -\int_{\Omega} \delta\sigma(s) \nabla_s G(x, s) \cdot \nabla_s G(s, y) ds, \end{aligned} \quad (4.14)$$

where we integrated by parts.

Next, let us use linearization in equation (4.8) to write the perturbation  $\delta\mathcal{K}_\sigma(x, y)$  of the kernel

$$\delta\mathcal{K}_\sigma(x, y) = \left( \frac{\delta\sigma(x)}{\sigma(x)} + \frac{\delta\sigma(y)}{\sigma(y)} \right) \mathcal{K}_\sigma(x, y) - \sigma(x)\sigma(y) \frac{\partial}{\partial\nu_x} \frac{\partial}{\partial\nu_y} \delta G(x, y). \quad (4.15)$$

Assuming that  $\delta\sigma|_{\mathcal{B}} = 0$ , we obtain from (4.15) and (4.14) that

$$\delta\mathcal{K}_\sigma(x, y) = \int_{\Omega} \delta\sigma(s) D\mathcal{K}_\sigma(s; x, y) ds, \quad (4.16)$$

with Jacobian

$$DK_\sigma(s; x, y) = \sigma(x)\sigma(y) \left( \nabla_s \frac{\partial}{\partial \nu_x} G(x, s) \right) \cdot \left( \nabla_s \frac{\partial}{\partial \nu_y} G(s, y) \right), \quad s \in \Omega. \quad (4.17)$$

Moreover, in the case  $\sigma \equiv 1$  used to compute the grids, we have

$$\nabla_s \frac{\partial}{\partial \nu_x} G(x, s) = \frac{1}{\pi|x-s|^2} \left( I - 2 \frac{(x-s)(x-s)^T}{|x-s|^2} \right) \nu(x), \quad (4.18)$$

$$\nabla_s \frac{\partial}{\partial \nu_y} G(s, y) = \frac{1}{\pi|y-s|^2} \left( I - 2 \frac{(y-s)(y-s)^T}{|y-s|^2} \right) \nu(y). \quad (4.19)$$

Now, let us derive similar sensitivity formulas for the discrete setting. Given the decomposition (2.3) of the Kirchhoff matrix, we note that the discrete equivalent of the Green's function is

$$G = -K_{II}^{-1} K_{IB}. \quad (4.20)$$

Denote by  $\gamma_k$  the conductances in our critical network, for  $k = 1, \dots, g$ , and  $g = n(n-1)/2$ . Note that the discrete DtN map  $\Lambda_\gamma \in \mathbb{R}^{n \times n}$  has precisely  $g$  degrees of freedom, since it is symmetric, and its diagonal is determined by the conservation of currents. Thus, the critical network, which is uniquely recoverable from  $\Lambda_\gamma$ , has as many conductances as the number of degrees of freedom of  $\Lambda_\gamma$ . We obtain by differentiating (2.5) with respect to  $\gamma_k$  that

$$\frac{\partial \Lambda_\gamma}{\partial \gamma_k} = \begin{bmatrix} G^T & I \end{bmatrix} \frac{\partial K}{\partial \gamma_k} \begin{bmatrix} G \\ I \end{bmatrix}. \quad (4.21)$$

But  $K$  is linear in  $\gamma$ , so the partial derivative  $\frac{\partial K}{\partial \gamma_k}$  is just the Kirchhoff matrix of a network with all the conductances being zero, except for  $\gamma_k = 1$ .

We denote by  $\text{vec}(M)$  the operation of stacking the entries in the strict upper triangular part of a matrix  $M \in \mathbb{R}^{n \times n}$  in a vector of size  $g$ . Then, we can form the Jacobian matrix  $D_\gamma \Lambda_\gamma \in \mathbb{R}^{g \times g}$ , with entries given by

$$(D_\gamma \Lambda_\gamma)_{jk} = \left( \text{vec} \left( \frac{\partial \Lambda_\gamma}{\partial \gamma_k} \right) \right)_j. \quad (4.22)$$

As the last step before defining the *sensitivity functions*, let us observe that the measurement operator  $\mathcal{M}_n$  can be viewed as acting on the kernel of the DtN map. This is obvious for the pointwise measurements (2.20), and for measurements (2.17) we have

$$(\mathcal{M}_n(DK_\sigma))_{ij}(s) = \begin{cases} \int_{\mathcal{B} \times \mathcal{B}} \chi_i(x) DK_\sigma(s; x, y) \chi_j(y) dx dy, & i \neq j, \\ - \sum_{k \neq i} \int_{\mathcal{B} \times \mathcal{B}} \chi_i(x) DK_\sigma(s; x, y) \chi_k(y) dx dy, & i = j. \end{cases} \quad (4.23)$$

**Definition 1.** *The sensitivity function of the conductance  $\gamma_k$  with respect to the changes in the conductivity  $\sigma$  is the  $k^{\text{th}}$  component of the vector function*

$$(D_\sigma \gamma)(s) = \left( D_\gamma \Lambda_\gamma |_{\Lambda_\gamma = \mathcal{M}_n(\Lambda_\sigma)} \right)^{-1} \text{vec}(\mathcal{M}_n(DK_\sigma)(s)), \quad s \in \Omega, \quad (4.24)$$

that we denote by  $(D_\sigma \gamma_k)(s)$ ,  $k = 1, \dots, g$ .

We are particularly interested in the sensitivity functions  $D_1 \gamma_k$  corresponding to  $\sigma \equiv 1$ . They are used to define the optimal grid, as explained next.

### 4.3. Definition of sensitivity grids.

Given the sensitivity functions (4.24), we define the points

$$S_{\alpha,\beta} = \arg \max_{s \in \Omega} (D\sigma \gamma_{k(\alpha,\beta)})(s), \quad (4.25)$$

where the solution  $\gamma_{k(\alpha,\beta)}$  of the discrete inverse problem is most sensitive to changes in the continuum conductivity  $\sigma$ . Here  $k$  is an indexing operator that stacks all the conductances in a vector in  $\mathbb{R}^g$ . If the maximum in (4.25) is attained at multiple points in  $\Omega$ , we define  $S_{\alpha,\beta}$  as the arithmetic average of those points. We use the points  $S_{\alpha,\beta}$  in (2.23), instead of the intersections  $P_{\alpha,\beta}$  of the unknown grid lines, and we call the grids with nodes  $S_{\alpha,\beta}$  the *sensitivity grids*.

Let us now illustrate the relationship between the points  $S_{\alpha,\beta}$  and  $P_{\alpha,\beta}$  in the case of full boundary measurements, where the optimal grid nodes  $P_{\alpha,\beta}$  are computed explicitly in [8, 27]. As mentioned in section 2.5, the optimal grid in this case is a tensor product of a uniform grid in the angular variable  $\theta$ , and an adaptive non-uniform optimal grid in the radial variable  $r$ . We show in figure 3 the optimal grids and the sensitivity functions for the circular networks used in [8, 27]. Note that the sensitivity functions of the conductances of various edges are mostly contained in the corresponding cells of the optimal grid. Moreover, the maxima  $S_{\alpha,\beta}$  (the yellow squares in figure 3) are almost indistinguishable from  $P_{\alpha,\beta}$  (the black circles in the figure).

### 4.4. The sensitivity grids for pyramidal networks

One can use the definition above to obtain sensitivity grids from any critical resistor network. However, not all network topologies give grids with good approximation properties. In particular, the numerical results in section 5 show that the pyramidal networks work better than the circular ones, for the partial data problem.

Note from figure 2 that in the pyramidal networks, the nodes  $v_1$  and  $v_n$  which delimit the accessible boundary  $\mathcal{B}_A$ , are separated by  $n-2$  interior nodes connected by the bottommost  $n-1$  horizontal edges that we associate with the inaccessible boundary  $\mathcal{B}_I$ . Thus, the number of nodes associated with  $\mathcal{B}_A$  and  $\mathcal{B}_I$  grow at the same rate as  $n$  increases. In comparison, *all* the boundary nodes of the circular networks [8, 27] are mapped in [11] to the accessible boundary conformally or quasiconformally. The conformal mappings preserve the isotropy of the conductivity, but give grids with poor resolution away from the center of  $\mathcal{B}_A$ . The quasiconformal grids have better resolution at the price of distortions in the reconstruction, due to the induced anisotropy of the conductivity. We believe that because the pyramidal networks allow the simultaneous growth of the sets of nodes in associated with  $\mathcal{B}_A$  and  $\mathcal{B}_I$ , they are better suited for partial data EIT. This is supported by the numerical results in section 5.

We illustrate in figure 4 the sensitivity functions  $D_1\gamma_k$  in the unit disk  $\mathbb{D}$ , for the pyramidal network with  $m = 4$  layers and  $n = 8$  boundary nodes. We use the notation  $(t, l, j)$  to index the edges of  $\Gamma_n$ . Here  $t \in \{h, v\}$  describes the type of the edge (horizontal/vertical), and  $l = 1, \dots, m$  determines the layer to which the edge belongs ( $l = m$  is the outermost layer). The edges in layer  $l$  are indexed by  $j$ , with  $j = 1, \dots, 2l-1$  for  $t = h$ , and  $j = 1, \dots, 2l-2$  for  $t = v$ .

The supports of the measurement functions  $\chi_j$ , used in (2.17) to define  $\mathcal{M}_n(\Lambda_1)$ , are centered at uniformly spaced points  $\theta_j \in \partial\mathbb{D}$ ,  $j = 1, \dots, n$ , on the accessible boundary  $\mathcal{B}_A = \{\theta \mid \theta \in (-\beta, \beta)\}$ . Note that  $\theta_j$  are symmetric with respect to the middle  $\theta = 0$  of the accessible boundary. This implies that  $\mathcal{M}_n(\Lambda_1)$  is symmetric with

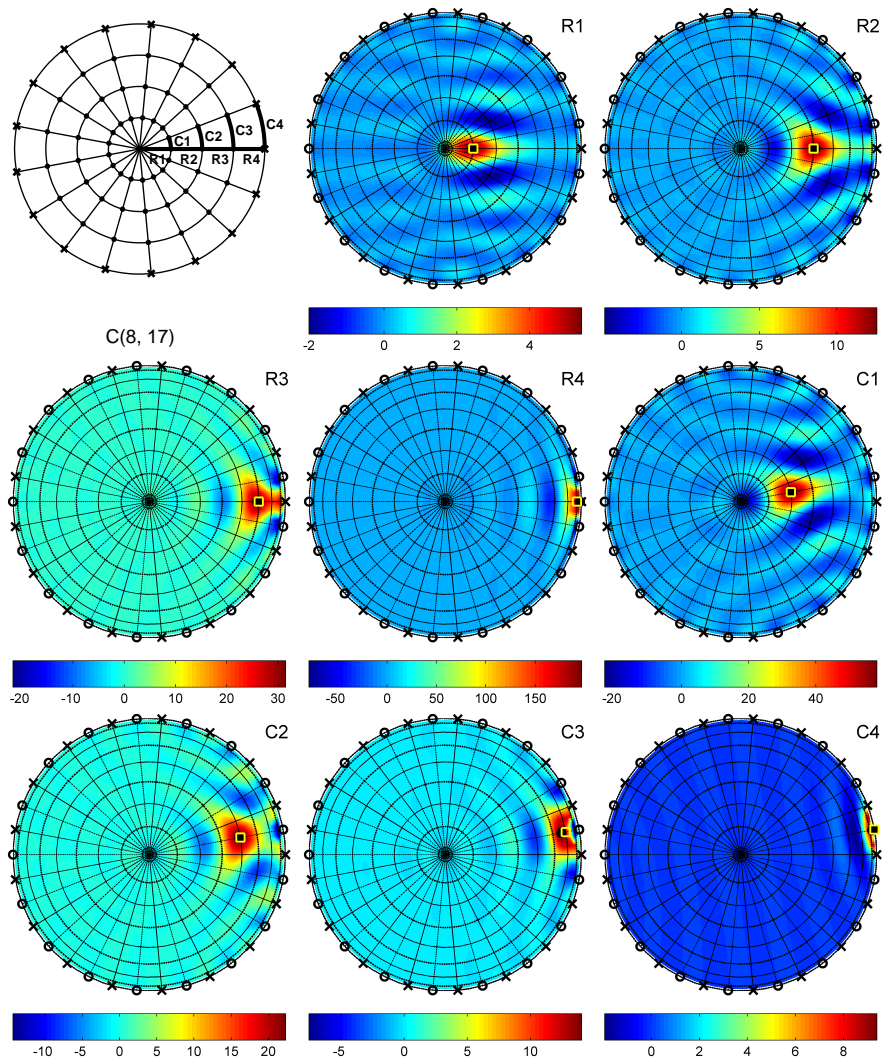


**Figure 3.** Sensitivity functions in  $\mathbb{D}$  corresponding to the circular network and a tensor product optimal grid. Top left: circular network with 8 layers,  $n = 17$ , boundary nodes are  $\times$ , sensitivities are computed for the edges  $R_1$ – $R_4$  and  $C_1$ – $C_4$  (bold). Left to right, top to bottom: sensitivity functions for the radial ( $R_1$ – $R_4$ ) and angular ( $C_1$ – $C_4$ ) conductances. Optimal grid lines: primary are solid, dual are dotted. Nodes  $P_{\alpha,\beta}$  are yellow  $\square$ ,  $S_{\alpha,\beta}$  are black  $\bullet$ .

respect to relabeling  $v_j \rightarrow v_{2m-j+1}$ ,  $j = 1, \dots, 2m$ , and so are the conductances. Thus, we only show in figure 4 the sensitivity functions for one half of the conductances in each layer  $l$ . The other half can be obtained from the symmetry  $\theta \rightarrow -\theta$ .

The sensitivity functions  $D_1 \gamma_k(s)$  shown in figure 4 have singularities near the supports of  $\chi_j$ . Once we “regularize” them, by setting them to zero in the vicinity of

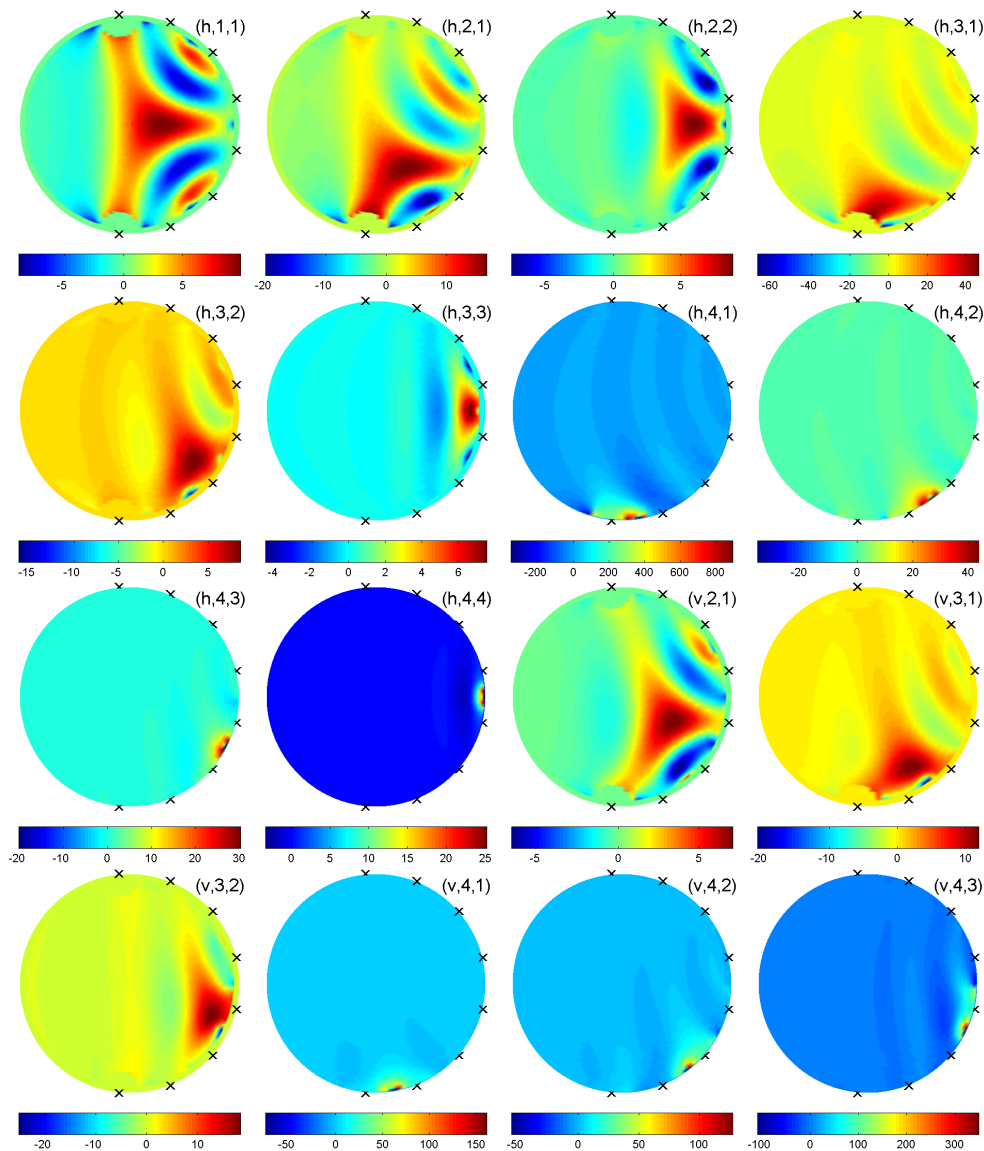


**Figure 4.** Sensitivity functions in  $\mathbb{D}$  for the pyramidal network with  $m = 4$ ,  $n = 8$ . The edges corresponding to each sensitivity function are indexed by  $(t, l, j)$ , where  $t \in \{h, v\}$  is the type of the edge (horizontal/vertical),  $l$  is the layer number and  $j$  is the index of the edge in the layer.  $\theta_j$  are  $\times$ ,  $\beta = 0.52\pi$ .

the singularities, we observe the well defined peaks that allow us to determine  $S_{\alpha,\beta}$ .

In figure 5 we show the grids obtained from the maxima of the regularized sensitivity function for two different sizes of the accessible boundary. While there is some grid refinement towards  $\mathcal{B}_A$ , the grids remain remarkably uniform deeper inside the domain. Note also that the neighboring points  $S_{\alpha,\beta}$  form very regular

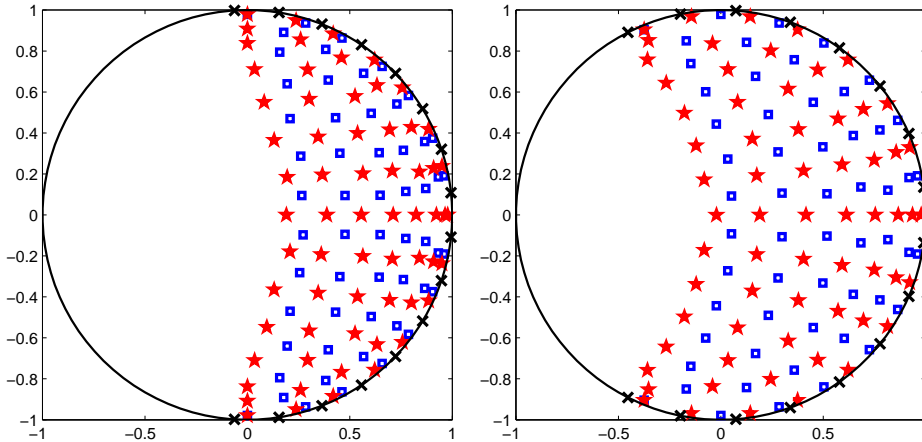


**Figure 5.** Sensitivity grids in  $\mathbb{D}$  for  $\Gamma_{16}$ . Left:  $\beta = 0.52$ ; right:  $\beta = 0.65$ . Blue  $\square$  correspond to vertical edges, red  $\star$  correspond to horizontal edges,  $\theta_j$  are black  $\times$ .

quadrilaterals, that are close to being rectangular. This is what is typically expected from grids with good approximation properties.

### 5. Reconstruction method and numerical results.

In this section we present the numerical results with pyramidal networks and sensitivity grids. The reconstruction algorithm is discussed in section 5.1. It is followed by a detailed description of the numerical experiments in section 5.2. The reconstructions are presented for the unit disk and for the half plane in sections 5.3 and 5.4, respectively. In the case of the unit disk, we compare the reconstructions with those obtained with the method in [11].

#### 5.1. Reconstruction algorithm.

Recall from section 2.5 that the reconstruction mapping  $\mathcal{Q}_n$  maps the data measurements  $\mathcal{M}_n(\Lambda_\sigma) \in \mathcal{D}_n$  to the set  $\mathcal{S}$  of positive and bounded conductivities. The algorithm that computes  $\mathcal{Q}_n(\mathcal{M}_n(\Lambda_\sigma))$  is as follows:

**Algorithm 2.** To compute the reconstruction  $\sigma^* = \mathcal{Q}_n(\mathcal{M}_n(\Lambda_\sigma))$  perform the following steps:

- (1) Let  $\beta$  be the size of the accessible boundary, and  $n$  the number of measurement functions  $\chi_j$ ,  $j = 1, \dots, n$ . Let  $\mathcal{M}_n(\Lambda_\sigma)$  be the measurements for the unknown conductivity. Compute  $\mathcal{M}_n(\Lambda_1)$  for the constant reference conductivity  $\sigma \equiv 1$ .
- (2) Solve the discrete inverse problem (2.22) using algorithm 1, to obtain the conductances  $\gamma_{\alpha,\beta}^{(1)}$ .
- (3) Use the solution of the discrete inverse problem from the previous step to compute the sensitivity functions  $D_1\gamma_{\alpha,\beta}^{(1)}$  as in (4.24). Compute the maxima  $S_{\alpha,\beta}$  of the regularized sensitivity functions.

- (4) Solve the discrete inverse problem (2.21) using algorithm 1, to obtain the conductances  $\gamma_{\alpha,\beta}$ .
- (5) Compute the reconstruction  $\sigma^*$  as the piecewise linear interpolation of the following quantities

$$\sigma^*(S_{\alpha,\beta}) = \frac{\gamma_{\alpha,\beta}}{\gamma_{\alpha,\beta}^{(1)}}. \quad (5.1)$$

We implement the piecewise linear interpolation of (5.1) by computing the Delaunay triangulation of  $S_{\alpha,\beta}$ . Then, the reconstruction is defined on the union  $T$  of triangles in the triangulation. In the case of the unit disk, we remove from  $T$  the triangles that have all three vertices at points  $S_{\alpha,\beta}$  corresponding to the bottommost chain of horizontal resistors in  $\Gamma_n$ . For each triangle in  $T$ , the vertex values of  $\sigma^*$  are interpolated by a linear function.

### 5.2. Numerical implementation.

In the first step of algorithm 2 we choose the number  $n$  of measurement functions, which is the same as the number of boundary nodes of the pyramidal network used for the reconstruction. The choice of  $n$  has been studied in detail in [8, 27] for the circular networks, and the results are applicable to the pyramidal networks as well. The main idea is that the instability of the continuum inverse problem manifests itself as the exponential ill-conditioning of the discrete problem. Layer peeling algorithms typically lose about one digit of accuracy per recovered layer. We regularize them by restricting  $n$  as explained in section 2.4. Note that in comparison with the circular networks, for which the number of layers is roughly one quarter of  $n$ , the pyramidal networks have a number of layers which is roughly  $n/2$ , which makes the layer peeling procedure less stable. Most of the numerical experiments presented below use noiseless data and pyramidal networks with  $n = 16$ , only for the less stable high contrast case we set  $n = 14$ . A numerical study of the noisy data case is presented in section 5.3.3.

For the reconstructions in the unit disk we use the same test conductivity functions as in [8, 27, 11]. The first one is a smooth function *sigX*, the other is a piecewise constant chest phantom *phantom1* [39]. Both conductivities are shown in figure 6. The high contrast conductivity used in section 5.3.4 is simply

$$\sigma(r, \theta) = \begin{cases} 1, & \theta \in [\frac{\pi}{2}, \frac{3\pi}{2}], \\ C_0, & \theta \in (0, \frac{\pi}{2}) \cup (\frac{3\pi}{2}, 2\pi), \end{cases} \quad (5.2)$$

where  $C_0$  is the contrast factor. In all cases the continuum data  $\Lambda_\sigma$  was approximated with a finite volume scheme on a very fine tensor product discretization grid (300 nodes in angular direction and 100 nodes in radial direction).

Since the sensitivity grids in figure 5 only resolve the conductivity in the region  $T$  that is slightly smaller than the convex hull of  $\mathcal{B}_A$ , we rotate the accessible boundary and the grid to focus the resolution on the different features of the test conductivities. The rotation parameter  $\omega_0$  is chosen in such way that the axis of symmetry of the grid is neither collinear nor orthogonal to the axes of symmetry of test conductivities.

We compare the reconstructions with those obtained by the method of extremal quasiconformal mappings [11]. The method is based on circular resistor networks, which are only recoverable for odd  $n$ . We let  $n = 17$  for the circular networks, which is close to  $n = 16$  used for the pyramidal networks. The method of extremal quasiconformal mappings is not very flexible with respect to the choice of the “measurement points”  $\theta_j$ . The locations of  $\theta_j$  are determined by  $n$ ,  $\beta$  and an additional

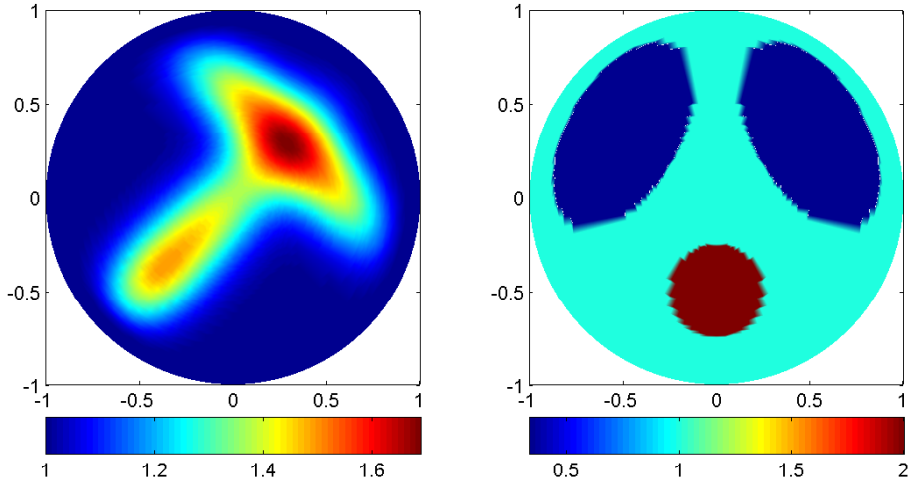


**Figure 6.** The conductivities used in the numerical experiments. Left: smooth conductivity *sigX*; right: piecewise constant chest phantom *phantom1*.

parameter specific to the method of [11], the artificial anisotropy factor  $K \in (0, 1]$ . It measures how much artificial anisotropy the method introduces to the solution, with smaller values of  $K$  corresponding to more anisotropy, and  $K = 1$  corresponding to the conformal mapping (no anisotropy). As a rule of thumb, the choice  $K \approx \beta/\pi$  gives a mapping with a close to uniform distribution of  $\theta_j$ . For the pyramidal networks, there are no limitations on the choice of  $\theta_j$ , which we distribute here uniformly on  $\mathcal{B}_A$ .

To quantify the quality of the reconstructions we introduce the pointwise relative error

$$E(z) = \left| \frac{\sigma^*(z)}{\sigma(z)} - 1 \right|, \quad z \in T, \quad (5.3)$$

and the mean relative error

$$[E] = \frac{\int_T E(z) dz}{\int_T dz} \cdot 100\%, \quad (5.4)$$

where  $T$  is defined in section 5.1. We show the value of  $[E]$  in the top right corner of the plots of the reconstructions.

### 5.3. Reconstructions in the unit disk.

We present below the reconstructions in  $\mathbb{D}$  for the smooth and piecewise constant conductivities of low and high contrasts. The reconstructions are computed for two sizes of the accessible boundary,  $\beta = 0.52\pi$  (slightly more than half of  $\partial\mathbb{D}$ ) and  $\beta = 0.65\pi$  (almost two thirds of  $\partial\mathbb{D}$ ).

*5.3.1. Reconstructions of smooth conductivity.* We begin in figure 7 with the reconstructions of the smooth conductivity, for  $\omega_0 = 6\pi/10$  and  $\omega_0 = 3\pi/10$ . Both

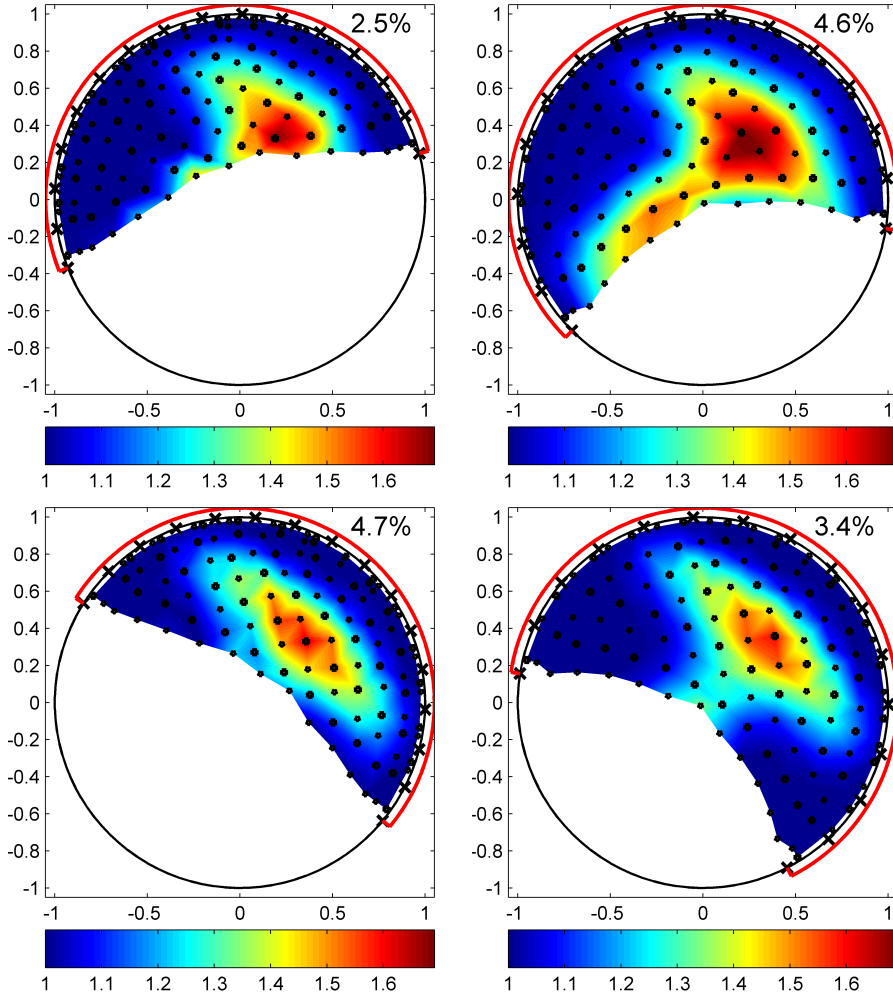


**Figure 7.** Reconstructions of smooth conductivity  $sigX$  with  $m = 8$ ,  $n = 16$ . Top row:  $\omega_0 = 6\pi/10$ ; bottom row:  $\omega_0 = 3\pi/10$ . Left column:  $\beta = 0.52\pi$ ; right column:  $\beta = 0.65\pi$ . Sensitivity grid nodes are  $\bullet$ ,  $\theta_j$  are  $\times$ ,  $\mathcal{B}_A$  is solid red. Percentages: mean relative errors  $[E]$ .

reconstructions capture the features of the conductivity without visible distortions of the geometry. There is a slight loss of contrast in the case  $\omega_0 = 3\pi/10$ , however the overall error  $[E]$  is still less than 5%.

In figure 8 we compare the reconstructions on the sensitivity grids with those obtained using a method of extremal quasiconformal mappings. As it was established in [11], the quality of the quasiconformal mapping reconstruction depends greatly on the size of the accessible boundary. If no artificial anisotropy is introduced ( $K = 1$ , the mapping is conformal), the measurement points are clustered towards the middle of  $\mathcal{B}_A$ , and the method fails to resolve away from the accessible boundary. If the artificial

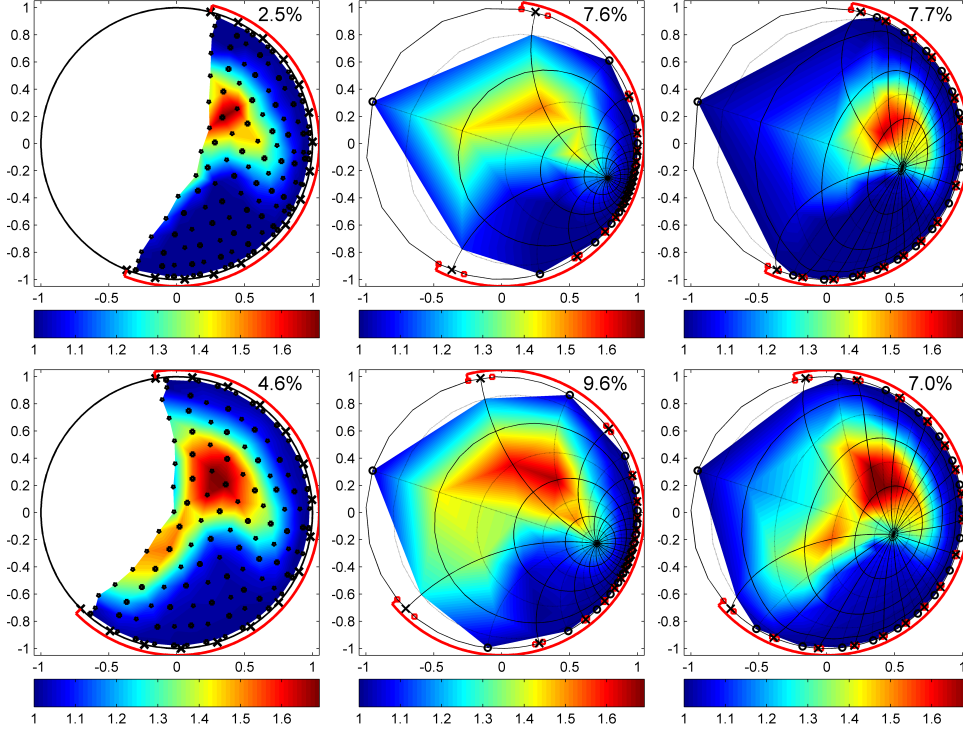


**Figure 8.** Comparison of reconstructions of smooth conductivity  $\text{sig}X$ ,  $\omega_0 = -\pi/10$ . Top row:  $\beta = 0.52\pi$ ; bottom row:  $\beta = 0.65\pi$ . Left column: reconstructions with pyramidal networks and sensitivity grids with  $m = 8$ ,  $n = 16$ ; middle column: conformal mapping reconstructions with  $n = 17$ ; right column: quasiconformal mapping reconstructions with  $n = 17$ ,  $K = 0.52$ (top),  $0.65$ (bottom).

anisotropy is allowed to spread  $\theta_j$  more uniformly throughout  $\mathcal{B}_A$ , the resolution is more uniform at the price of some distortions in the geometry of the reconstruction.

We observe in figure 8 that in the case  $\beta = 0.52\pi$ , both the conformal and quasiconformal reconstructions have a mean relative error that is three times larger than that of the reconstruction on the sensitivity grid. As we expand  $\mathcal{B}_A$  to  $\beta = 0.65\pi$ , the quasiconformal solution shows some improvement, but it still has a larger error  $[E]$ . Thus, the approach with pyramidal networks and sensitivity grids is superior, because it gives a uniform resolution, and it does not introduce any distortions.

**5.3.2. Reconstructions of piecewise constant conductivity.** Let us now consider reconstructions of the piecewise constant chest phantom. We refer to the low and high conductivity regions of the phantom as the lungs and the heart, respectively. In figure 9, we show the reconstructions for  $\omega_0 = 4\pi/10$  and  $\omega_0 = \pi/10$ .

We observe that the reconstructions have a much larger error  $[E]$  compared to those for the smooth conductivity  $\text{sig}X$ . This is due to an analogue of the Gibbs phenomenon, as the method overestimates or underestimates the discontinuous

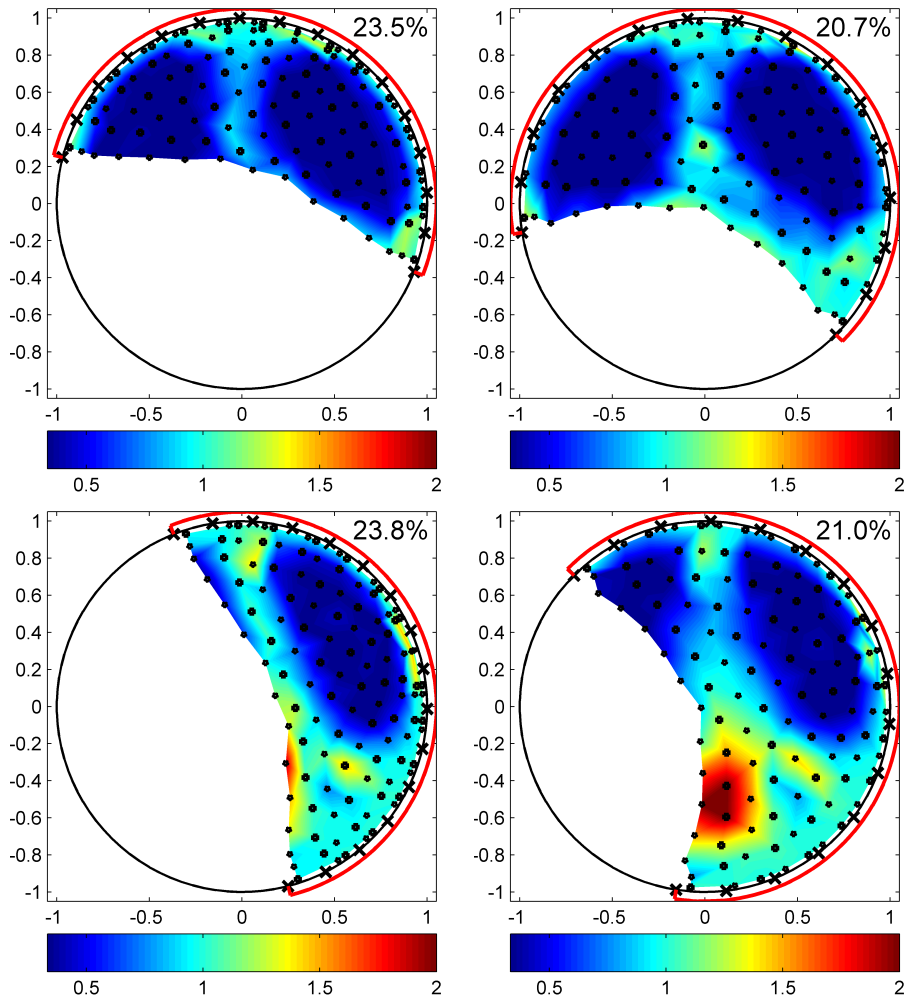


**Figure 9.** Reconstructions of piecewise constant conductivity *phantom1* with  $m = 8$ ,  $n = 16$ . Top row:  $\omega_0 = 4\pi/10$ ; bottom row:  $\omega_0 = \pi/10$ . Left column:  $\beta = 0.52\pi$ ; right column:  $\beta = 0.65\pi$ . Sensitivity grid nodes are  $\bullet$ ,  $\theta_j$  are  $\times$ ,  $\mathcal{B}_A$  is solid red. Percentages: mean relative errors  $[E]$ .

conductivity near the interfaces of discontinuity $\|$ . In figure 9, this phenomenon is more pronounced in the case  $\omega_0 = \pi/10$ , especially for  $\beta = 0.52\pi$ , where we observe three overshoots near the right lung.

In figure 10, we compare the performance of our method with the method of extremal quasiconformal mappings. Similar to the case of smooth conductivity, the reconstructions on the sensitivity grids are superior, with a mean relative error that is half of the error of the conformal and quasiconformal reconstructions.

$\|$  These oscillations may be removed later, by adding a total variation penalty term when implementing the Gauss-Newton iteration to solve (2.24), as was done in [8, 27].

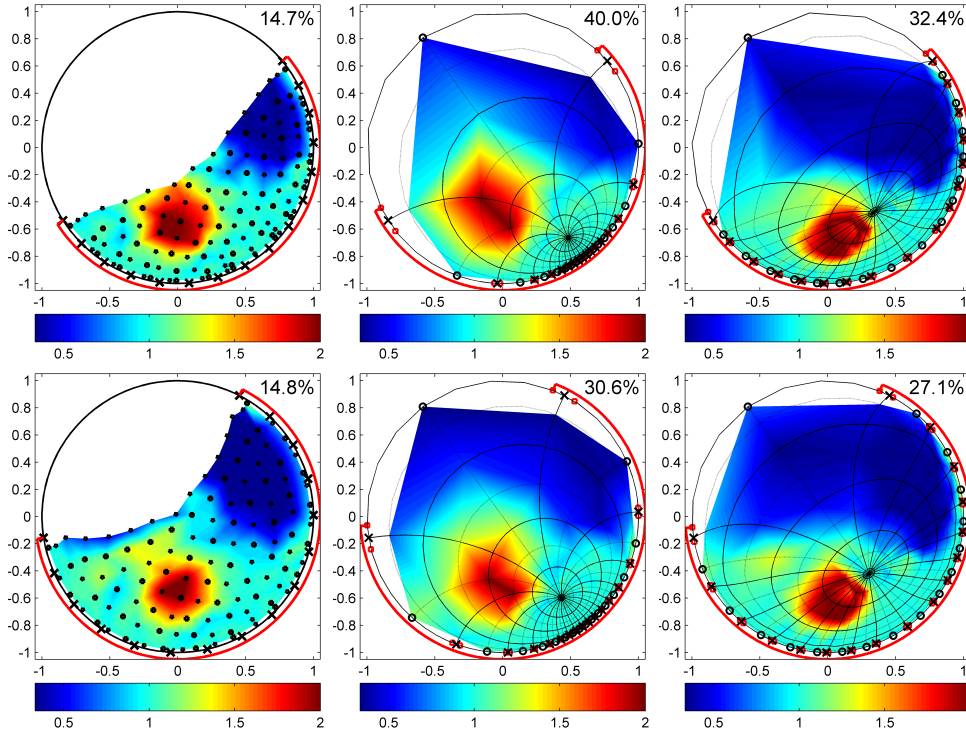


**Figure 10.** Comparison of reconstructions of piecewise constant conductivity *phantom1*,  $\omega_0 = -3\pi/10$ . Top row:  $\beta = 0.52\pi$ ; bottom row:  $\beta = 0.65\pi$ . Left column: reconstructions with pyramidal networks and sensitivity grids with  $m = 8$ ,  $n = 16$ ; middle column: conformal mapping reconstructions with  $n = 17$ ; right column: quasiconformal mapping reconstructions with  $n = 17$ ,  $K = 0.52$ (top),  $0.65$ (bottom).

*5.3.3. Noisy data reconstructions.* Following [8] we study the reconstructions from noisy data by adding multiplicative mean zero Gaussian noise to the approximated kernel of  $\Lambda_\sigma$ . Then we choose the largest network size  $n$  for which algorithm 1 yields positive conductances. In table 1 we present mean relative errors  $[E]$  for the reconstructions from the noisy data in the same setting as in the top row of figure 10 for a typical realization of Gaussian noise.

Noise level	0%	0.1%	0.5%	1%	5%
$n$	16	12	10	10	8
Error $[E]$	14.7%	15.9%	17.2%	18.6%	19.0%

**Table 1.** Noisy data reconstruction errors. Piecewise constant conductivity *phantom1*,  $\omega_0 = -3\pi/10$ ,  $\beta = 0.52\pi$ .

As expected from the exponential ill-conditioning of the problem, the network size quickly decreases. However, the reconstruction error  $[E]$  does not grow exponentially

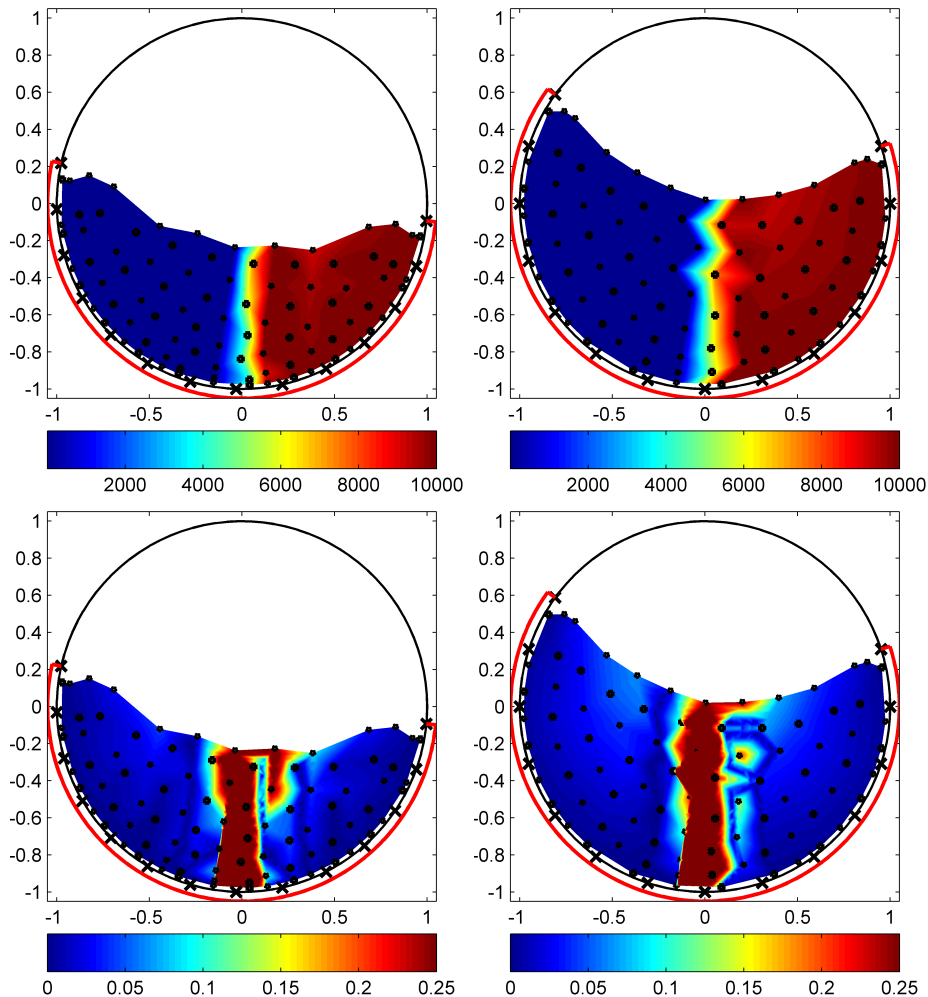


**Figure 11.** Reconstructions of high contrast piecewise constant conductivity with  $m = 7$ ,  $n = 14$ ,  $\omega_0 = -11\pi/20$ . Top row: reconstructions; bottom row: pointwise relative error  $E(z)$ . Left column:  $\beta = 0.52$ ; right column:  $\beta = 0.65$ . Sensitivity grid nodes are  $\bullet$ ,  $\theta_j$  are  $\times$ ,  $\mathcal{B}_A$  is solid red.

with the noise level.

*5.3.4. High contrast reconstructions.* An advantage of the reconstruction mapping based on resistor networks is that it is obtained from the full non-linear inverse problem, without artificial regularization, aside from limiting the size of the networks. Thus, it avoids the problems of many other approaches, that often struggle to recover high contrast features of  $\sigma(x)$ . The numerical results in this section show that our reconstructions capture contrasts that are orders of magnitude larger than those recoverable by traditional approaches.

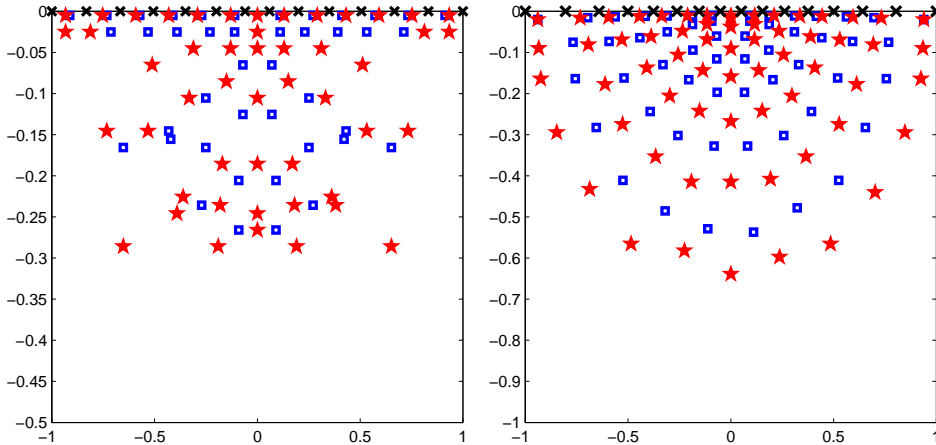


**Figure 12.** Optimal grids in the half plane. Left: sensitivity grid computed directly ( $n = 14$ ); right: sensitivity grid mapped conformally from the unit disk ( $n = 16$ ). Blue  $\square$  correspond to vertical edges, red  $\star$  correspond to horizontal edges, measurement points  $x_j$  are black  $\times$ .

In the top row of figure 11 we present reconstructions of the piecewise constant conductivity 5.2, with exceptionally large contrast  $C_0 = 10^4$ . The mean relative error does not give a clear estimate of the quality of the reconstruction for such a large contrast, so we use the pointwise relative error  $E(z)$  instead, which we show in the bottom row of figure 11.

Our method is able to capture both the location of the interface of discontinuity and the values of the conductivity on both sides of the interface. While the relative error is large near the interface due to the spurious oscillations, away from the interface the error is less than 5%. Note that these reconstructions are achieved without any special assumptions on the conductivity, which shows the versatility of the method.

#### 5.4. Reconstructions in the half plane.

We already mentioned in section 4.4 that the pyramidal networks are better suited for the partial data EIT problem, because of the fixed ratio of the number of nodes associated with the accessible and inaccessible parts of the boundary. The sensitivity grids obtained from these networks have good approximation properties for order one ratios of the accessible and inaccessible boundary, as illustrated with the numerical results above. When this ratio approaches infinity, we are basically in the full boundary measurement case, where the circular networks are more appropriate [8, 27, 11]. Here we discuss the other limit, where the ratio tends to zero. This limit arises when considering the EIT problem in the lower half plane  $\mathbb{R}_-^2$ , with measurements limited to a finite segment of the horizontal axis.

Let  $\mathcal{B}_A = [-1, 1]$  be the accessible boundary, and let the “measurement points”  $x_j \in \mathcal{B}_A$  be the centers of the supports of the measurement functions  $\chi_j(x)$ . It was observed in [11] that the distribution of the measurement points had a profound

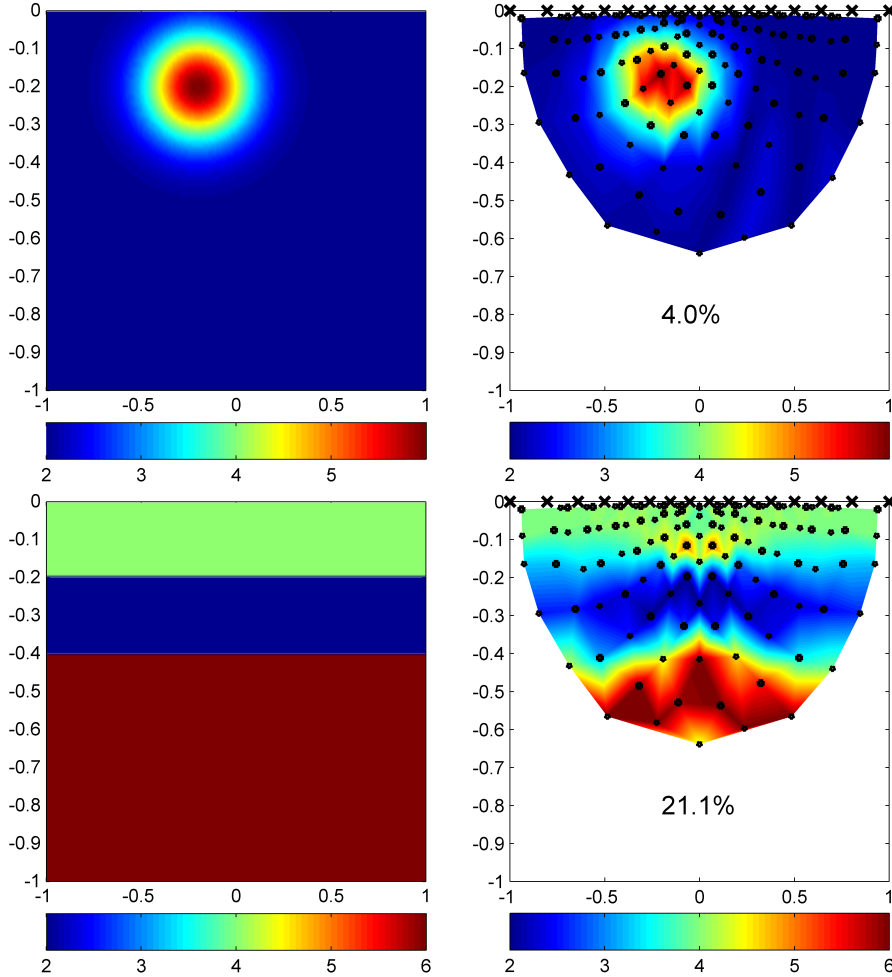


**Figure 13.** Reconstruction in the half plane with  $m = 8$ ,  $n = 16$ . Top row: smooth conductivity  $\sigma_g$ ; bottom row: piecewise constant conductivity  $\sigma_l$ . Left column: true conductivities; right column: reconstructions. Grid nodes are  $\bullet$ ,  $x_j$  are black  $\times$ , percentages are  $[E]$ .

influence on the optimal grids obtained with circular networks. Here we show that the same is true for the pyramidal ones.

If we attempt to compute the sensitivity grid for an arbitrarily chosen distribution of  $x_j$ , it will likely have poor properties for inversion. See for example the grid shown in the left plot in figure 12. To get a good grid, in this limit case of zero ratio of accessible to inaccessible boundary, we use conformal mappings. Explicitly, we map conformally a grid that has good properties in one domain (e.g. the unit disk with measurements at points  $\theta_j$ , uniformly distributed on half of the boundary) to the half plane, with measurements in  $\mathcal{B}_A$ . We use conformal mappings to preserve the isotropy of the conductivity and the angles of the grid lines, as explained in [11].

The grid in the right plot in figure 12 is obtained with the conformal fractional linear transform  $w : \mathbb{D} \rightarrow \mathbb{R}_-^2$  given by

$$w(z) = ih \frac{\bar{z} - 1}{\bar{z} + 1}, \quad h = \tan\left(\frac{\pi - \beta}{2}\right), \quad (5.5)$$

for which the distribution of  $x_j$  is

$$x_j = h \cot\left(\frac{\pi - \theta_j}{2}\right), \quad j = 1, \dots, n. \quad (5.6)$$

We observe that the distribution of the nodes of the resulting grid is very regular, and there is greater penetration depth compared to that of the grid computed directly from the regularized sensitivity functions. The numerical reconstructions in figure 13 are obtained with the conformally mapped grid.

Similar to the study in  $\mathbb{D}$ , we reconstruct both a smooth and a piecewise constant conductivity in  $\mathbb{R}_-^2$ . The smooth conductivity  $\sigma_g$  consists of a single inclusion in the homogeneous background medium modeled by a Gaussian. The piecewise constant conductivity  $\sigma_l$  has three horizontal layers. Both test conductivities are shown in the left column in figure 13. The reconstructions are shown in the right column.

As in the case of the unit disk, we observe a much smaller error  $[E]$  for the reconstruction of a smooth conductivity compared to that of the reconstruction of the piecewise constant  $\sigma_l$ . While both the position and the magnitude of the Gaussian inclusion are determined with high precision, the magnitude of the middle layer of  $\sigma_l$  is somewhat overestimated, and there are also two symmetric overshoots in the top layer. However, the overall quality of the reconstruction is comparable to what we observe in the unit disk, which shows that our method is versatile with respect to the choice of the domain.

## 6. Summary

We have introduced a novel reconstruction method for two dimensional electrical impedance tomography (EIT) with partial boundary measurements. The reconstruction is to be used in the inversion algorithm presented in [8, 27]. It is based on a model reduction approach that encodes the information about the unknown conductivity function  $\sigma$  in few parameters. As in [8, 27, 11], the reduced models are well connected, critical resistor networks that arise in finite volumes discretizations of the elliptic partial differential equation for the potential. The networks are consistent with the discrete measurements of the Dirichlet to Neumann (DtN) map  $\Lambda_\sigma$ , and since they are critical (they have no redundant connections), they are uniquely recoverable from them. The *pyramidal* network topology considered here is different than the *circular* one in [8, 27, 11], and it is better suited for the partial measurement setup.

We have shown the unique solvability of the inverse problem for pyramidal resistor networks, and have introduced a layer peeling algorithm that recovers them from the measurements  $\mathcal{M}_n(\Lambda_\sigma)$  of the DtN map at  $n$  boundary points, in a finite number of algebraic steps. We regularize the algorithm by limiting the size of the network, thus obtaining a sparse parametrization of the unknown conductivity function.

The reconstruction of  $\sigma$  amounts to defining a mapping  $\mathcal{Q}_n$ , from the measurements  $\mathcal{M}_n(\Lambda_\sigma)$  to the set of positive and bounded scalar conductivity functions. This mapping is obtained from the conductances of the pyramidal network (the reduced model), interpreted as averages of  $\sigma$  on an *optimal grid*.

Unlike the optimal grids introduced in [4, 21, 22, 30] for forward problems, or the ones considered in [7, 8, 27, 11] for inverse problems, the grids defined here are truly two dimensional. We call them *sensitivity optimal* grids because they are computed using the sensitivity functions of conductances of pyramidal networks obtained by solving the inverse problem for measurements  $\mathcal{M}_n(\Lambda_1)$ . These grids are defined so that finite volumes approximations on them compute the measurements of the DtN map *exactly* for the case of constant conductivity  $\sigma \equiv 1$ . What is crucial for inversion is that they have very good extrapolation properties for a wide class of conductivity functions, not just  $\sigma \equiv 1$ . This is why the reconstruction mapping defined on them is an approximate inverse of the forward map, and can be used as a preconditioner in the inversion algorithm [8, 27].

We have demonstrated the versatility of our reconstruction approach with numerical simulations that include cases of discontinuous conductivity with exceptionally high contrast. We have also compared our results with those given by an alternative approach presented in a recent paper [11]. The method in [11] shows how to extend the reconstruction method introduced in [8, 27] to the partial measurements case. It uses circular resistor networks and extremal quasiconformal mappings to transform the problem with measurements on the accessible boundary  $\mathcal{B}_A \subset \mathcal{B}$  to one with measurement points distributed uniformly on the entire boundary  $\mathcal{B}$ . It is shown in [11] that the restriction of the measurements to  $\mathcal{B}_A$  induces a coordinate transformation of the optimal grids resulting from the circular networks, which must be undone by the quasiconformal mappings. This in turn induces an artificial anisotropy of the transformed conductivity, which is why the reconstructions have distortions. The smaller  $\mathcal{B}_A$  is, the worse the reconstructions in [11].

Our motivation for this paper came from the realization that the problems of the reconstructions in [11] are due to the essentially one dimensional structure of the optimal grids, and the inadequate topology of the reduced models, the circular resistor networks, for the partial measurements setup. The pyramidal networks presented here are much better suited for this problem. The resulting two dimensional grids are far superior to those in [11], in terms of distribution and refinement properties in the domain, and they give more accurate reconstructions.

### Acknowledgements

The work of L. Borcea was partially supported by the National Science Foundation, grants DMS-0604008, DMS-0934594, DMS-0907746 and by the Office of Naval Research grant N000140910290. The work of A. Mamonov was partially supported by the National Science Foundation, grants DMS-0604008, DMS-0934594 and by Schlumberger Technology Corporation under the research agreement R62860.

### Appendix A. Proof of Lemma 1.

Our proof is based on the observation that the pyramidal graphs have a self similarity property. If we remove (peel) the layer of edges of  $\Gamma_n$  that emanate from the boundary nodes, the resulting graph is  $\Gamma_{n-2}$ . The number of layers that we can peel until no edges are left is  $m$ , and it is related to the number of boundary nodes as  $n = 2m$  or  $n = 2m - 1$ . Here we give the proof in the case of even  $n$ . Its extension to odd  $n$  is straightforward.



**Figure A1.** Unique connections for maximal circular pairs  $(P; Q)$  for induction base case  $n = 4$ . Nodes in  $P$  are  $\circ$ , nodes in  $Q$  are  $\times$ .

*Proof.* To prove that the network is critical we must construct for every edge  $e \in E$  a circular pair  $(P_e; Q_e) \in \pi(\Gamma_n)$ , such that the connection between  $P_e$  and  $Q_e$  is broken when  $e$  is removed (deleted) from  $\Gamma_n$ . We do so in two steps. First, we show that circular pairs  $(P; Q)$  of maximal size  $|P| = |Q| = m$  are uniquely connected. Then, we demonstrate how to construct such a pair, whose unique connection passes through a given edge  $e$ . Therefore, the deletion of  $e$  must break the connection.

**Unique connectivity of maximal circular pairs:** We show by induction over  $n = 2m$  that any circular pair  $(P; Q)$  of maximal size  $|P| = |Q| = m$  is uniquely connected through  $\Gamma_n$ . Since

$$|P| + |Q| = 2m = n = |Y_B|,$$

we have  $Y_B = P \cup Q$  and we can write, without loss of generality,

$$P = \{v_{s+1}, \dots, v_{s+m}\}, \quad Q = \{v_{s+m+1}, \dots, v_{2m}, v_1, \dots, v_s\}, \quad (\text{A.1})$$

for some integer  $s$  satisfying  $1 < s \leq m$ . The induction step is 4, so we consider two base cases:  $n = 2$  and  $n = 4$ . The case  $n = 2$  is trivial, because  $\Gamma_2$  is a single resistor connecting the two boundary nodes  $v_1$  and  $v_2$ . In the case  $n = 4$  there exist two maximal circular pairs (up to swapping  $P$  and  $Q$ )  $P = \{v_2, v_3\}$ ,  $Q = \{v_1, v_4\}$ , and  $P = \{v_3, v_4\}$ ,  $Q = \{v_1, v_2\}$ . The unique connections are illustrated in figure A1.

Now, the subgraphs  $\Gamma_j$  of  $\Gamma_n$ , for  $j = 2, 4, \dots, n - 2$ , are obtained by repeated peeling of the layers of edges adjacent to the boundary, and subsequent relabeling of the nodes adjacent to the peeled edges as boundary nodes. In particular, we obtain  $\Gamma_{n-4}$  by peeling two layers from  $\Gamma_n$ .

The inductive hypothesis says that every maximal circular pair  $(P'; Q')$  of  $\Gamma_{n-4}$  is connected by a unique set of disjoint paths in  $\Gamma_{n-4}$ . To show that the maximal pair (A.1) of  $\Gamma_n$  is uniquely connected through the graph  $\Gamma_n$ , we must show that  $(P; Q)$  must be connected to a maximal pair  $(P'; Q')$  of  $\Gamma_{n-4}$ , which we denote by

$$P' = \{w_s, w_{s+1}, \dots, w_{s+m-3}\}, \quad Q' = \{w_{s+m-2}, \dots, w_{2m-4}, w_1, \dots, w_{s-1}\}. \quad (\text{A.2})$$

Furthermore, the connection is unique. The construction is illustrated in figure A2, and we distinguish two cases.

**The case  $1 < s < m$ :** The connection is constructed starting with  $v_1, v_{2m} \in Q$ . Since these nodes are connected to  $\Gamma_n$  by horizontal edges only, these edges must be added to the connecting paths. Moreover, the paths must continue along horizontal edges to  $w_1$  and  $w_{2m-4}$ , because if we take vertical edges, we reach the boundary nodes  $v_2, v_{2m-1}$ , that we are not allowed to touch.

Next, we observe that there is a unique way of connecting  $v_2$  and  $v_{2m-1}$  to  $w_2$  and  $w_{2m-5}$ , which is also by horizontal edges. Indeed, if we added the vertical edges to

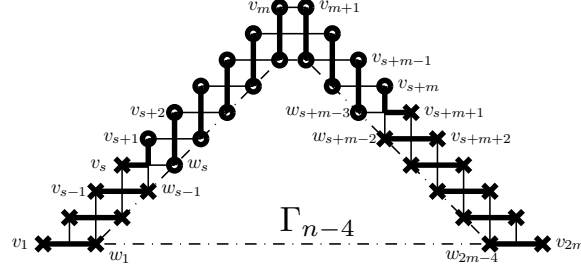


**Figure A2.** Induction step from  $\Gamma_{n-4}$  to  $\Gamma_n$ : connection between  $(P; Q)$  and  $(P'; Q')$ . Nodes in  $P$  and  $P'$  are  $\circ$ , nodes in  $Q$  and  $Q'$  are  $\times$ . Edges not in the connection are thin solid, edges in the connection are thick solid. Dash-dotted lines bound  $\Gamma_{n-4}$  (not actual edges).

the paths, the paths would intersect with the horizontal edges added at the previous step. Similarly, we build the paths connecting the nodes from  $Q$  to  $Q'$ , until we reach  $v_s$  and  $v_{s+m+1}$ . Arguing as before, all the edges must be horizontal.

It remains to connect the nodes in  $P$ . We start from  $v_m, v_{m+1} \in P$ , and since they are not allowed to be connected by a common horizontal edge, we add two vertical edges to the paths. The next two edges must also be vertical, otherwise the paths would either intersect, or touch the boundary at  $v_{m-1}$  or  $v_{m+2}$ . We repeat this argument for other nodes in  $P$  until we reach  $v_{s+1}$  and  $v_{s+m}$ . For each of the nodes  $v_{s+1} \in P$  and  $v_{s+m} \in P$  we add one vertical edge, at which point they meet with the horizontal edges added for  $v_s \in Q$  and  $v_{s+m+1} \in Q$ , which completes the paths for these two pairs of nodes.

Thus, we have constructed the paths between  $v_{s+1} \in P$  and  $v_s \in Q$ , and between  $v_{s+m} \in P$  and  $v_{s+m+1} \in Q$ , while the remaining nodes in  $P$  and  $Q$  are connected by a unique set of paths (horizontal for  $Q$ , vertical for  $P$ ) to the nodes in  $P'$  and  $Q'$ . Invoking the induction hypothesis for the maximal pair  $(P'; Q')$  in  $\Gamma_{n-4}$ , we conclude that  $(P; Q)$  is connected by a unique set of paths through  $\Gamma_n$ , for  $1 < s < m$ .

**The case  $s = m$ :** Arguing as above, the nodes of  $P = \{v_{m+1}, \dots, v_{2m}\}$  and  $Q = \{v_1, \dots, v_m\}$  are connected to  $P'$  and  $Q'$  by horizontal edges, since  $v_1 \in Q$  and  $v_{2m} \in P$ . A circular pair  $(P'; Q')$  has the form  $P' = \{w_{m-1}, \dots, w_{2m-4}\}$ ,  $Q' = \{w_1, \dots, w_{m-2}\}$ , and  $v_m \in Q$  is connected to  $v_{m+1} \in P$  by a common horizontal edge. Then, the result follows by the induction hypothesis for the maximal pair  $(P'; Q')$  in  $\Gamma_{n-4}$ .

**Connection through a given edge:** To complete the proof we need to show how to construct a maximal circular pair  $(P_e; Q_e)$  for any given edge  $e$ , such that the unique connection passes through  $e$ . First, consider a horizontal edge  $e$ . As we showed above for  $P = \{v_{m+1}, \dots, v_{2m}\}$  and  $Q = \{v_1, \dots, v_m\}$ , the unique connection passes through all horizontal edges of  $\Gamma_n$ . Thus, the deletion of any horizontal edge breaks the connection.

Let  $e = (t, b)$  be a vertical edge with end nodes  $t$  (top) and  $b$  (bottom). We follow the vertical edges from  $t$  up to the boundary node  $p$ , that we add to  $P_e$ . We also consider a horizontal line of edges passing through node  $b$ . We denote the boundary

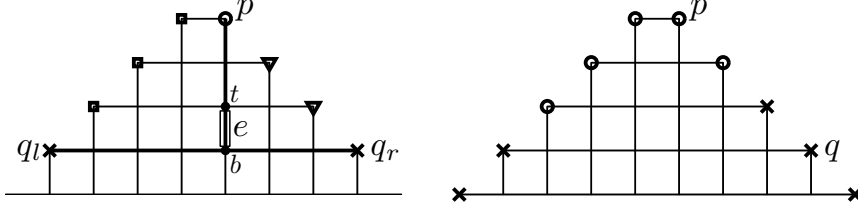


**Figure A3.** Left: two circular subsets of boundary nodes to choose from. Nodes in an even subset are  $\nabla$ , nodes in the odd subset are  $\square$ . Right: construction of  $(P_e, Q_e)$ , nodes in  $P_e$  are  $\circ$ , nodes in  $Q_e$  are  $\times$ .

end nodes of this line by  $q_l \in B$  (left one) and  $q_r \in B$  (right one), as shown in the left plot in figure A3.

Consider a subgraph of  $\Gamma_n$  consisting of its upper part lying on and above the horizontal line of edges connecting  $q_l$  and  $q_r$ . This subgraph is itself pyramidal with an even number of boundary nodes. Thus, one of the two subsets of boundary nodes lying either between  $p$  and  $q_r$ , or between  $q_l$  and  $p$ , must have an even number of nodes (zero is considered even). We choose the subset with even number of nodes and let  $q$  be either  $q_r$  or  $q_l$  depending on which subset we chose. Then, we add  $q$  to  $Q_e$ .

The rest of  $P_e$  and  $Q_e$  is populated as follows. Consider the two circular subsets of boundary nodes between  $p$  and  $q$ , and between  $q$  and  $p$ . Both subsets have an even number of nodes. Half of the nodes in each subset we add to  $P_e$ , and another half we add to  $Q_e$ , depending on whether the node is closest to  $p$  or  $q$ , respectively. This is illustrated in figure A3.

Now, we have constructed the maximal pair  $(P_e; Q_e)$ , which must be connected by a unique set of  $m$  disjoint paths, as proved at step 1. Moreover, the path from  $p$  to  $q$  must consist of the following two segments: the line of vertical edges from  $b$  to  $p$  (this includes  $e$ ), and the line of horizontal edges from  $b$  to  $q$ . Indeed, since  $p \in P_e$ , the construction of the unique path (step 1) shows that it should be connected to  $P'_e$  by vertical edges, which in turn is also connected to  $P''_e$  by vertical edges, and so on. Here we use the notation at step 1, with  $P'_e$  the set of  $m - 2$  points on the boundary of  $\Gamma_{n-4}$ , and  $P''_e$  the set of  $m - 4$  points on the boundary of  $\Gamma_{n-8}$ .

A similar argument for  $q \in Q_e$  shows that its segment of the path consists of the horizontal edges. By the construction of  $p$  and  $q$ , these two path segments intersect at  $b$ . Finally, since the connection for  $(P_e; Q_e)$  is unique, and the path between  $p \in P_e$  and  $q \in Q_e$  contains  $e \in E$ , deleting  $e$  from  $\Gamma_n$  breaks the connection, which completes the proof.  $\square$

## Appendix B. Proof of Theorem 1.

The outline of the proof is as follows. First, we show that *special solutions* corresponding to the excitations defined at steps 1 and 2 of the algorithm, if they exist, give a unit potential drop on the edges emanating from the boundary node  $v_p$ . Then, we show the existence of such solutions. Finally, we establish formula (3.3) for the updated DtN map.

*Proof.*

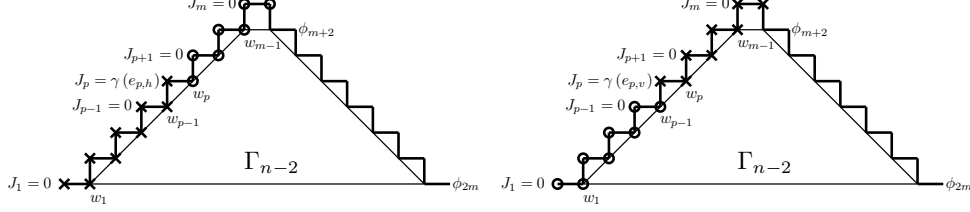


**Figure B1.** Special solutions. Left: special solution for  $\gamma(e_{p,h})$ ; right: special solution for  $\gamma(e_{p,v})$ . Nodes with zero potential are  $\circ$ , nodes with unit potential are  $\times$ . Edges to be peeled are thick solid. Narrow solid lines bound  $\Gamma_{n-2}$  (not actual edges).

**Special solutions with unit potential drop:** Recall that  $Y_B = \{v_1, \dots, v_{2m}\}$  is the set of boundary nodes of  $\Gamma_n$ , and  $S = \{w_1, \dots, w_{2m-2}\}$  is the set of boundary nodes of  $\Gamma_{n-2}$ . This is the subgraph of  $\Gamma_n$  obtained by peeling the edges emanating from the nodes in  $Y_B$ . Let  $e_{p,h} = (v_p, w_p)$ ,  $e_{p,v} = (v_p, w_{p-1})$  be the horizontal and vertical edges emanating from  $v_p \in Y_B$ .

We construct the special solutions  $u^{(p,h)}$  and  $u^{(p,v)}$  so that the potential drop on  $e_{p,h}$  and  $e_{p,v}$  is one, and we can recover  $\gamma(e_{p,h})$  and  $\gamma(e_{p,v})$  from the measured current  $J_p^{(h)}$  and  $J_p^{(v)}$ , respectively. The behavior of the special solutions is illustrated in figure B1.

Consider first the case  $1 \leq p \leq m$ , and begin the construction of the special solution  $u^{(p,h)}$  by setting the boundary conditions. The boundary conditions are stated in terms of the following subsets of  $Y_B$ :  $H = \{v_1, \dots, v_p\}$ ,  $Z = \{v_1, \dots, v_{p-1}, v_{p+1}, \dots, v_m\}$ ,  $F = \{v_{p+1}, \dots, v_{m+1}\}$  and  $C = \{v_{m+2}, \dots, v_{2m}\}$ . If we denote by  $\phi$  the boundary potential, then its restriction to  $C$ , denoted by  $\phi_C$ , is determined from the combination of Dirichlet and Neumann data

$$\begin{cases} \phi_H &= 1, \\ \phi_F &= 0, \\ J_Z &= 0. \end{cases} \quad (\text{B.1})$$

This is shown later in the proof, where we establish the existence of special solutions.

Now, let us denote by  $\psi$  the restriction of the potential to  $S$ . The current at the boundary node  $v_j$  is given by

$$J_j = \gamma(e_{j,h})(\phi_j - \psi_j) + \gamma(e_{j,v})(\phi_j - \psi_{j-1}), \quad (\text{B.2})$$

for all nodes in  $Y_B$ , except  $v_1$  and  $v_{2m}$ , where only the first term is present. This is because there is only one horizontal edge emanating from each of these two nodes. We show by induction that  $u^{(p,h)}$ , the potential drop on  $e_{p,h}$  is one, and the drop on  $e_{p,v}$  is zero. Thus, according to (B.2),

$$\gamma(e_{p,h}) = J_p^{(h)}. \quad (\text{B.3})$$

Let us first show that  $\psi_{p-1} = 1$ . Since  $v_1 \in Z \cap H$ , equation (B.2) for  $j = 1$  gives

$$0 = J_1^{(h)} = \gamma(e_{1,h})(1 - \psi_1), \quad \text{therefore} \quad \psi_1 = 1.$$

Next, we proceed by induction in  $j = 2, \dots, p-1$ ,  $v_j \in Z \cap H$ . Suppose that  $\psi_{j-1} = 1$ , then (B.2) becomes

$$0 = \gamma(e_{j,h})(1 - \psi_j),$$

which becomes  $\psi_{p-1} = 1$  for  $j = p-1$ .

Now we use another induction argument to show that  $\psi_p = 0$ . Since  $v_m \in Z \cap F$  and  $v_{m+1} \in F$ , equation (B.2) for  $j = m$  gives

$$0 = J_m^{(h)} = \gamma(e_{m,h})(\phi_m - \phi_{m+1}) + \gamma(e_{m,v})(\phi_m - \psi_{m-1}) = -\gamma(e_{m,v})\psi_{m-1},$$

thus  $\psi_{m-1} = 0$ . We proceed by induction in  $j = m-1, \dots, p+1$ , where  $v_j \in Z \cap F$ . Suppose that  $\psi_j = 0$ , then (B.2) gives

$$0 = \gamma(e_{j,v})(0 - \psi_{j-1}),$$

and if we set  $j = p+1$ , we get  $\psi_p = 0$ . We have just established that  $\psi_{p-1} = 1$ ,  $\psi_p = 0$ , and since  $\phi_p = 1$ , (B.3) holds.

To determine  $\gamma(e_{p,v})$  we construct a special solution  $u^{(p,v)}$  in a similar manner. The sets  $Z$  and  $C$  are the same as for  $u^{(p,h)}$ , while  $V = \{v_p, \dots, v_{m+1}\}$  and  $F = \{v_1, \dots, v_{p-1}\}$ . The boundary conditions are determined by (B.1), with  $H$  replaced by  $V$ . An induction argument similar to the one above, shows that the potential drop on  $e_{p,h}$  is zero, and the drop on  $e_{p,v}$  is one. Thus,

$$\gamma(e_{p,v}) = J_p^{(v)}. \quad (\text{B.4})$$

**Existence of special solutions:** We now establish the existence of solutions with boundary conditions (B.1), by converting them to Dirichlet conditions, for which existence and uniqueness is known [15]. Since conditions on  $\phi_H$  and  $\phi_F$  are Dirichlet, we need to convert  $J_Z = 0$  to a Dirichlet condition on  $\phi_C$ ,  $C = Y_B \setminus (H \cup F)$ . We rewrite  $J_Z = 0$  using the DtN map as

$$0 = \Lambda_{Z,F}^{(n)}\phi_F + \Lambda_{Z,H}^{(n)}\phi_H + \Lambda_{Z,C}^{(n)}\phi_C, \quad (\text{B.5})$$

which is combined with (B.1) to get

$$\phi_C = -\left(\Lambda_{Z,C}^{(n)}\right)^{-1} \Lambda_{Z,H} \mathbf{1}_H, \quad (\text{B.6})$$

where  $\mathbf{1}_H$  is a column vector of ones of size  $|H|$ . Thus, the question of existence of the special solution is equivalent to  $\det \Lambda_{Z,C}^{(n)} \neq 0$ .

To show the invertability of  $\Lambda_{Z,C}^{(n)}$ , we use the result from [15, Theorem 4.2], which says that for a circular pair  $(P; Q)$  with  $|P| = |Q| = k$ , the condition  $(-1)^k \det \Lambda_{P,Q} > 0$  is satisfied if and only if  $(P; Q)$  is connected through the network, otherwise  $\det \Lambda_{P,Q} = 0$ . We demonstrate that  $(Z; C) \in \pi(\Gamma_n)$  by constructing the connection explicitly, as shown in figure B2.

For  $j = 1, \dots, p-1$  we connect  $v_j \in Z$  and  $v_{2m-j+1} \in C$  with paths of horizontal edges. For  $j = p+1, \dots, m$  we connect  $v_j \in Z$  and  $v_{2m-j+2} \in C$  with paths consisting of one vertical edge  $e_{j,v} = (v_j, w_{j-1})$  and a path of horizontal edges connecting  $w_{j-1}$  and  $v_{2m-j+2}$ .

Recall that so far we considered the case  $1 \leq p \leq m$ . The case  $m+1 \leq p \leq 2m$  is similar. In fact, since  $\Gamma_n$  is symmetric with respect to the vertical axis, the argument becomes identical to the previous one if we relabel the boundary nodes  $v_j \rightarrow v_{2m-j+1}$ ,

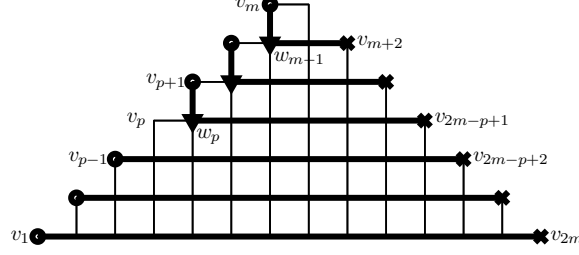


**Figure B2.** Connection for  $(Z; C)$ . Nodes in  $Z$  are  $\circ$ , nodes in  $C$  are  $\times$ . The paths are thick solid lines, edges not in the paths are narrow solid lines. Nodes at the intersections of vertical and horizontal path segments are  $\nabla$ .

$j = 1, \dots, 2m$ . This exhausts all possible  $v_p \in B$ , and we can finally obtain the formulas (3.1)–(3.2) by substituting (B.6) into

$$J_p = \Lambda_{p,H}^{(n)} \phi_H + \Lambda_{p,C}^{(n)} \phi_C, \quad \text{and} \quad J_p = \Lambda_{p,V}^{(n)} \phi_V + \Lambda_{p,C}^{(n)} \phi_C.$$

**DtN map update formula:** Once we know the conductances of the edges emanating from  $Y_B$ , we peel the outer layer and reduce the inverse problem to the one for the smaller network  $(\Gamma_{n-2}, \gamma)$ . It remains to derive the DtN map  $\Lambda^{(n-2)} \in \mathbb{R}^{(n-2) \times (n-2)}$  of this network.

We rewrite equation (2.5) using the specific structure of the DtN map of  $(\Gamma_n, \gamma)$ . The graph  $\Gamma_n$  consists of  $m$  layers of nodes. Each layer is a set of boundary nodes of  $\Gamma_{2j}$ ,  $j = 1, \dots, m$ . The layer  $j$  is connected by paths of length one only to the two adjacent layers  $j - 1$  and  $j + 1$  (except for  $j = 1, m$ ). Thus, the Kirchhoff matrix  $K$  of  $(\Gamma_n, \gamma)$  has a block tridiagonal structure

$$K = \begin{bmatrix} K_{11} & K_{12} & 0 & \cdots & 0 \\ K_{21} & K_{22} & K_{23} & \cdots & 0 \\ 0 & K_{32} & \ddots & \ddots & \vdots \\ \vdots & \vdots & \ddots & K_{SS} & K_{SB} \\ 0 & 0 & \cdots & K_{BS} & K_{BB} \end{bmatrix} = \begin{bmatrix} K_{II} & K_{IB} \\ K_{BI} & K_{BB} \end{bmatrix}. \quad (\text{B.7})$$

Here  $K_{jj} \in \mathbb{R}^{2j \times 2j}$ ,  $j = 1, \dots, m$ , are the diagonal blocks with  $K_{m-1, m-1} = K_{SS}$ ,  $K_{m, m} = K_{BB}$ . Furthermore,  $K_{j, j+1} \in \mathbb{R}^{2j \times (2j+2)}$ ,  $K_{j, j+1} = K_{j+1, j}^T$ ,  $j = 1, \dots, m - 1$ , are the off-diagonal blocks corresponding to connections between the layers  $j$  and  $j + 1$ .

Using (B.7) we rewrite (2.5) as

$$\Lambda^{(n)} = K_{BB} - K_{BS} (K_{II}^{-1})_{SS} K_{SB}. \quad (\text{B.8})$$

We can also relate the potential  $\phi$  at the boundary  $Y_B$  of  $\Gamma_n$  to the potential  $\psi$  at the boundary  $S$  of  $\Gamma_{n-2}$  via

$$K_{BS} \psi = (\Lambda^{(n)} - K_{BB}) \phi. \quad (\text{B.9})$$

Recall that the matrix of the DtN map is defined as the current response for boundary potential excitations that are the columns of an identity matrix. Thus, we rewrite (B.9)

in matrix form with an identity matrix  $\Psi = I_{n-2}$  and an unknown  $\Phi \in \mathbb{R}^{n \times (n-2)}$ , to obtain an overdetermined matrix equation

$$K_{BS} = (\Lambda^{(n)} - K_{BB})\Phi, \quad (\text{B.10})$$

that we now show to be solvable.

Note that once we recover the conductance for the edges emanating from  $Y_B$ , we know the blocks  $K_{BS}$  and  $K_{BB}$  of the Kirchhoff matrix  $K$ . Let  $M = (\Lambda^{(n)} - K_{BB})$ , and obtain from (B.8) that

$$M = -K_{BS} (K_{II}^{-1})_{SS} K_{SB}. \quad (\text{B.11})$$

To show that (B.10) is solvable, we need to show that  $M$  is full rank. We do so by considering a block LDU decomposition of  $K_{II}$ . Since  $K_{II}$  is block tridiagonal, it admits a decomposition

$$K_{II} = \begin{bmatrix} I & 0 & & \\ L_1 & I & \ddots & \\ & \ddots & \ddots & 0 \\ & & L_{m-2} & I \end{bmatrix} \begin{bmatrix} D_1 & 0 & & \\ 0 & D_2 & \ddots & \\ & \ddots & \ddots & 0 \\ & & 0 & D_{m-1} \end{bmatrix} \begin{bmatrix} I & U_1 & & \\ 0 & I & \ddots & \\ & \ddots & \ddots & U_{m-2} \\ & & 0 & I \end{bmatrix}, \quad (\text{B.12})$$

where all blocks  $D_j$ ,  $j = 1, \dots, m-1$ , are non-singular, because  $K_{II}$  is invertible. If we denote the diagonal blocks of  $K_{II}^{-1}$  by  $Z_j$ ,  $j = 1, \dots, m-1$ , it can be shown [23, 25, 44] that they satisfy

$$Z_{m-1} = D_{m-1}^{-1}, \quad (\text{B.13})$$

$$Z_j = D_j^{-1} + U_j Z_{j+1} L_j, \quad j = m-2, \dots, 1. \quad (\text{B.14})$$

Of particular interest to us is (B.13), which gives  $Z_{m-1} = D_{m-1}^{-1} = (K_{II}^{-1})_{SS}$ , hence  $(K_{II}^{-1})_{SS}$  is invertible. Since  $\Gamma_n$  is connected, the blocks  $K_{BS}$  and  $K_{SB}$  are full rank. This establishes that  $M$  is of full rank.

We can now solve equation (B.10). Let  $P \in \mathbb{R}^{(n-2) \times n}$  be a full rank projector, so that  $PP^T = I_{n-2}$ . Then, if we search for  $\Phi$  in the form  $\Phi = P^T \widehat{\Phi}$ , we obtain from (B.10) that

$$PK_{BS} = PMP^T \widehat{\Phi}, \quad (\text{B.15})$$

$$\widehat{\Phi} = P^T (PMP^T)^{-1} PK_{BS}. \quad (\text{B.16})$$

The final step in deriving  $\Lambda^{(n-2)}$  is to write the Kirchhoff law for the nodes in  $S$ . If  $G = Y_I \setminus S$ , then

$$K_{SG} u_G + (K_S + K_G) \psi + K_{SB} \phi = 0, \quad (\text{B.17})$$

where we split  $K_{SS}$  in two parts  $K_{SS} = K_S + K_G$ , corresponding to the edges connecting  $S$  to  $Y_B$  and  $S$  to  $G$ , respectively. The DtN map of  $(\Gamma_{n-2}, \gamma)$  is then the current from  $S$  to  $B$ , given by

$$J_{SB} = -K_S \psi - K_{SB} \phi,$$

which we rewrite in matrix form using  $\Psi = I_{n-2}$  and (B.16), to obtain (3.3).  $\square$

## References

- [1] G. Alessandrini. Stable determination of conductivity by boundary measurements. *Applicable Analysis*, 27(1):153–172, 1988.
- [2] A. Allers and F. Santosa. Stability and resolution analysis of a linearized problem in electrical impedance tomography. *Inverse Problems*, 7:515–533, 1991.
- [3] K. Astala and L. Päivärinta. Calderón’s inverse conductivity problem in the plane. *Annals of Mathematics-Second Series*, 163(1):265–300, 2006.
- [4] S. Asvadurov, V. Druskin, and L. Knizhnerman. Application of the difference Gaussian rules to solution of hyperbolic problems. *Journal of Computational Physics*, 158(1):116–135, 2000.
- [5] J.A. Barcelo, T. Barcelo, and A. Ruiz. Stability of the inverse conductivity problem in the plane for less regular conductivities. *Journal of Differential Equations*, 173(2):231–270, 2001.
- [6] L. Borcea. Electrical impedance tomography. *Inverse Problems*, 18(6):99–136, 2002.
- [7] L. Borcea and V. Druskin. Optimal finite difference grids for direct and inverse Sturm-Liouville problems. *Inverse Problems*, 18(4):979–1002, 2002.
- [8] L. Borcea, V. Druskin, and F. Guevara Vasquez. Electrical impedance tomography with resistor networks. *Inverse Problems*, 24(3):035013 (31pp), 2008.
- [9] L. Borcea, V. Druskin, and L. Knizhnerman. On the Continuum Limit of a Discrete Inverse Spectral Problem on Optimal Finite Difference Grids. *Communications on Pure and Applied Mathematics*, 58(9):1231, 2005.
- [10] L. Borcea, V. Druskin, and A. Mamonov. Solving the discrete EIT problem with optimization techniques, 2007. Schlumberger-Doll Report.
- [11] L. Borcea, V. Druskin, and A.V. Mamonov. Circular resistor networks for electrical impedance tomography with partial boundary measurements. Accepted for publication in *Inverse Problems*, 2010.
- [12] R.M. Brown and G. Uhlmann. Uniqueness in the inverse conductivity problem for nonsmooth conductivities in two dimensions. *Commun. Partial Diff. Eqns*, 22:1009–27, 1997.
- [13] A.P. Calderón. On an inverse boundary value problem, Seminar on Numerical Analysis and its Applications to Continuum Physics, Soc. *Brasileira de Matematica, Rio de Janeiro*, pages 65–73, 1980.
- [14] E. Curtis, E. Mooers, and J.A. Morrow. Finding the conductors in circular networks from boundary measurements. *RAIRO - Mathematical Modelling and Numerical Analysis*, 28:781–814, 1994.
- [15] E.B. Curtis, D. Ingerman, and J.A. Morrow. Circular planar graphs and resistor networks. *Linear Algebra and its Applications*, 23:115–150, 1998.
- [16] E.B. Curtis and J.A. Morrow. *Inverse problems for electrical networks*. World Scientific, 2000.
- [17] Y.C. de Verdière. Reseaux electriques planaires I. *Commentarii Mathematici Helvetici*, 69(1):351–374, 1994.
- [18] Y.C. de Verdière, I. Gitler, and D. Vertigan. Reseaux electriques planaires II. *Commentarii Mathematici Helvetici*, 71(1):144–167, 1996.
- [19] V. Druskin. The unique solution of the inverse problem of electrical surveying and electrical well-logging for piecewise-continuous conductivity. *Izv. Earth Physics*, 18:51–3, 1982.
- [20] V. Druskin. On uniqueness of the determination of the three-dimensional underground structures from surface measurements with variously positioned steady-state or monochromatic field sources. *Sov. Phys.-Solid Earth*, 21:210–4, 1985.
- [21] V. Druskin and L. Knizhnerman. Gaussian spectral rules for second order finite-difference schemes. *Numerical Algorithms*, 25(1):139–159, 2000.
- [22] V. Druskin and L. Knizhnerman. Gaussian spectral rules for the three-point second differences: I. A two-point positive definite problem in a semi-infinite domain. *SIAM Journal on Numerical Analysis*, 37(2):403–422, 2000.
- [23] I.S. Duff, A.M. Erisman, and J.K. Reid. *Direct methods for sparse matrices*. Oxford University Press, USA, 1986.
- [24] H.W. Engl, M. Hanke, and A. Neubauer. *Regularization of inverse problems*. Kluwer Academic Pub, 1996.
- [25] A.M. Erisman and W.F. Tinney. On computing certain elements of the inverse of a sparse matrix. *Communications of the ACM*, 18(3):177–179, 1975.
- [26] L.C. Evans. *Partial Differential Equations*. AMS, 1997.
- [27] F. Guevara Vasquez. *On the Parametrization of Ill-posed Inverse Problems Arising from Elliptic Partial Differential Equations*. PhD thesis, Rice University, Houston, TX, USA, 2006.
- [28] O.Y. Imanuvilov, G. Uhlmann, and M. Yamamoto. Global uniqueness from partial Cauchy data in two dimensions. *Arxiv preprint arXiv:0810.2286*, 2008.

- [29] D. Ingerman. Discrete and continuous Dirichlet-to-Neumann maps in the layered case. *SIAM Journal on Mathematical Analysis*, 31:1214–1234, 2000.
- [30] D. Ingerman, V. Druskin, and L. Knizhnerman. Optimal finite difference grids and rational approximations of the square root I. Elliptic problems. *Communications on Pure and Applied Mathematics*, 53(8):1039–1066, 2000.
- [31] D. Ingerman and J. A. Morrow. On a characterization of the kernel of the Dirichlet-to-Neumann map for a planar region. *SIAM Journal on Applied Mathematics*, 29:106–115, 1998.
- [32] D. Isaacson. Distinguishability of conductivities by electric current computed tomography. *IEEE transactions on medical imaging*, 5(2):91–95, 1986.
- [33] K. Knudsen, M. Lassas, J.L. Mueller, and S. Siltanen. Regularized d-bar method for the inverse conductivity problem. *Inverse Problems and Imaging*, 3:599–624, 2009.
- [34] R. Kohn and M. Vogelius. Determining conductivity by boundary measurements. *Communications on Pure and Applied Mathematics*, 37:289–98, 1984.
- [35] R. Kohn and M. Vogelius. Determining conductivity by boundary measurements II. Interior results. *Communications on Pure and Applied Mathematics*, 38(5), 1985.
- [36] H.R. MacMillan, T.A. Manteuffel, and S.F. McCormick. First-order system least squares and electrical impedance tomography: part II. *To appear*.
- [37] H.R. MacMillan, T.A. Manteuffel, and S.F. McCormick. First-order system least squares and electrical impedance tomography. *SIAM Journal on Numerical Analysis*, 42(2):461–483, 2004.
- [38] N. Mandache. Exponential instability in an inverse problem for the Schrodinger equation. *Inverse Problems*, 17(5):1435–1444, 2001.
- [39] J.L. Mueller, S. Siltanen, and D. Isaacson. A direct reconstruction algorithm for electrical impedance tomography. *IEEE Trans. Med. Imaging*, 21(6):555–559, 2002.
- [40] A.I. Nachman. Global uniqueness for a two-dimensional inverse boundary value problem. *Annals of Mathematics*, pages 71–96, 1996.
- [41] AD Seagar, DC Barber, and BH Brown. Theoretical limits to sensitivity and resolution in impedance imaging. *Clinical Physics and Physiological Measurement*, 8:13–31, 1987.
- [42] E. Somersalo, M. Cheney, and D. Isaacson. Existence and uniqueness for electrode models for electric current computed tomography. *SIAM Journal on Applied Mathematics*, 52(4):1023–1040, 1992.
- [43] J. Sylvester. An anisotropic inverse boundary value problem. *Communications on Pure and Applied Mathematics*, 43(2):201–232, 1990.
- [44] K. Takahashi, J. Fagan, and M.S. Chen. Formation of a sparse bus impedance matrix and its application to short circuit study. In *Power Industry Computer Applications Conference*, pages 63–69, 1973.